UNIVERSITÉ DU QUÉBEC À RIMOUSKI

HYDRODYNAMIQUE DE LA BAIE DE SEPT-ÎLES

MÉMOIRE PRÉSENTÉ

dans le cadre du programme de maîtrise en océanographie

en vue de l'obtention du grade de M. Sc.

PAR

Juin 2019

Composition du jury :

Cédric Chavanne, président du jury, Université du Québec à Rimouski

Daniel Bourgault, directeur de recherche, Université du Québec à Rimouski

Dany Dumont, codirecteur de recherche, Université du Québec à Rimouski

Frédéric Cyr, examinateur externe, Pêches et Océans Canada

UNIVERSITÉ DU QUÉBEC À RIMOUSKI

Service de la bibliothèque

Avertissement

Il continue à fixer la mer. Silence. De temps en temps, il trempe le pinceau dans une tasse de cuivre et trace sur la toile quelques traits légers. Les soies du pinceau laissent derrière elles l'ombre d'une ombre très pâle que le vent sèche aussitôt en ramenant la blancheur d'avant. De l'eau. Dans la tasse de cuivre il n'y a que de l'eau.

- Extrait de *Océan mer*,
  Alessandro Baricco

Simon et Chamou, vous avez rempli chaque jour de chaleur, de douceur, de rire et d'aventure. Je vous en remercie du fond du coeur. À Florence, tu en sais probablement beaucoup plus sur la baie de Sept-Îles que ce que ton intérêt motive ! Je te remercie de m'avoir écouté avec patience. Je te remercie aussi d'avoir été une partenaire indéfectible pendant ma maîtrise et d'avoir vaillamment enduré trois ans de relation à distance pour que ton copain aille à l'école.

RÉSUMÉ

Les variabilités tidale et saisonnière de la température, la salinité et les courants ont été mesurées dans la baie de Sept-Îles (BSI) du printemps à l'automne 2017 et au printemps 2018. Des bouées dérivantes et des profileurs ADCP ont été déployés pour mesurer les courants et des profils CTDs ont été récoltés 5 fois à 21 stations réparties dans la baie et l'archipel. Des passages répétés pendant 12 h le long d'un transect à l'embouchure ont été réalisés avec un ADCP en route. Durant cette mesure, des arrêts réguliers ont été faits pour collecter des profils CTDs. Les courants moyennés sur un cycle de marée étaient vers l'aval près de la surface (0-5 m) et généralement vers l'amont en eau plus profonde (15-50 m). Un courant vers l'aval a été mesuré près de Pointe à la Marmite tout au long du cycle de marée et apparaît aussi dans les données de bouées dérivantes. Les vitesses moyennes et maximales de bouées dérivantes sont de 17.4 cm s^{-1} et 86.6 cm s^{-1}. Leur cap était en moyenne 24±39° à l'ouest du cap du vent et elles se sont échouées sur les plages opposées aux directions des vents dominants (NNW et ESE) dans 22/46 des cas. Un courant anti-cyclonique à l'échelle de la baie a été mesuré à marée montante et la circulation de surface était cyclonique en moyenne près de la surface au jusant. La perturbation saisonnière de stratification était à son plus fort au début du mois de juin et son influence était surtout sentie dans les 20 m sous la surface. Le temps de résidence de la BSI est estimé entre 2-12 jours. Le rayon interne de Rossby est calculé à L_D = 2.8 km et L_D = 6.8 km en stratification respectivement faible et forte, suggérant que l'effet de la rotation de la terre sur l'hydrodynamique ne peut pas être négligé. Une critique du modèle conceptuel existant de la circulation dans la BSI est émise, ainsi que des recommandations en vue d'un nouveau modèle.

Mots clés : Baies fermées, dynamique des baies, observations, milieux côtiers

ABSTRACT

Seasonal and tidal variability of temperature, salinity, and currents were measured in the bay of Sept-Îles (BSI) from spring to fall 2017, and in spring 2018. Surface drifters and ADCP profilers were deployed to measure current velocities and CTD profiles were recorded regularly at 21 stations spread out across the bay and archipelago. Repeated passages along a transect at the bay mouth were conducted during 12 hours with an underway ADCP. During these transects, regular stops were made for CTD profiling. Tidally-averaged currents were out-flowing near the surface (0-5 m) and generally in-flowing in deeper waters (15-50 m). A seaward current was measured near Pointe à la Marmite throughout the tidal cycle and also appears in drifter data. Surface drifter speeds average to 17.4 cm s^{-1} but reached up to 86.6 cm s^{-1}. Drifter heading was 24±39° west of wind direction on average and they shoaled on beaches leeward of dominant winds (NNW and ESE) in 22/46 cases. A bay scale anti-cyclonic current was measured at rising tide and surface circulation during ebb was cyclonic on average. Seasonal disturbance of stratification was strongest in early June and was mostly felt in the top 20 meters. Bulk residence time for water in the BSI is scaled to 2-12 days. The internal Rossby radius is scaled to L_D = 2.8 km and L_D = 6.8 km during low and high stratification, suggesting influence of earth's rotation on hydrodynamics can not be neglected. Criticism of the existing conceptual model for circulation in the BSI, and a starting point for a new model are given.

Keywords : Enclosed bays, bay dynamics, observations, coastal waters

TABLE DES MATIÈRES

LISTE DES TABLEAUX

LISTE DES FIGURES

INTRODUCTION GÉNÉRALE

Motivation

L'évaluation objective de la santé d'un écosystème peut s'avèrer une tâche complexe, surtout en présence d'un biôme richement diversifié comme on en trouve souvent dans les baies (Greenlaw et al., 2011). Pour surveiller la santé globale des écosystèmes en ne considérant qu'un sous-ensemble fini de leurs paramètres, des indices de santé écologiques sont développés notamment en Europe (Birk et al., 2012) et dans une variété d'endroits (Halpern et al., 2008), visant une application locale.

L'indice de santé des océans (OHI) développé par Halpern et al. (2012) est un exemple de ces méthodes. Afin de chiffrer la santé d'un écosystème, sa réponse aux stress anthropique, biologique et climatique est d'abord utilisée pour prédire son état futur. Une comparaison entre cet état futur et un état de référence sain évalue son état de santé présent. Il est toutefois connu que les indices de santé écologiques sont peu fiables à l'extérieur des écosystèmes pour lesquels ils ont été développés (Gillett et al., 2015).

En contexte d'une présence humaine croissante aux latitudes arctiques et sub-arctiques, il y a aussi un besoin croissant de développer des outils pour aider les décideurs à gérer de façon durable et informée par la science. Pour répondre à ce besoin, une étude multi-disciplinaire a été conduite dans le cadre du partenariat stratégique *Canadian Healthy Oceans Network* (CHONe) en collaboration avec l'Institut nordique de recherche en environnement en santé au travail (INREST) visant à développer un indice de santé écologique adapté à la baie de Sept-Îles (BSI).

Objectifs

Les différents facteurs de stress qui agissent sur la santé d'un écosystème le font d'une façon hautement interactive, c'est pourquoi une approche intégratrice des paramètres chimiques, biologiques et physiques est à favoriser (Halpern et al., 2012). Vecteur de transport de tous les paramètres physico-chimiques marins, la circulation de l'eau est un élément clé de la dynamique de ces interactions. Elle peut notamment évacuer, retenir, concentrer ou importer des contributions au stress anthropique. Une compréhension quantitative de l'hydrodynamique de la BSI est une étape incontournable à franchir en vue de développer des indicateurs écologiques performants pour cette aire d'étude. L'objectif de ce projet est de construire un jeu de données suffisant pour résoudre et quantifier dans la BSI la variabilité des paramètres physiques à l'échelle tidale et saisonnière, et pour permettre la validation et calibration de modèles hydrodynamiques.

La baie de Sept-Îles

Fortement industrialisée et sujette à un traffic maritime international, la BSI se trouve à proximité d'écosystèmes semblables (Baie Sainte-Marguerite, Baie Moisie) qui sont moins sujets à l'influence humaine, faisant de ce locus un endroit pratique pour étudier l'effet du stress anthropique sur les communautés benthiques et pélagiques en climat sub-arctique.

La BSI (figure 1) est située dans le nord-ouest du golfe du Saint-Laurent (GSL) à 50°N. Une comparaison entre la largeur de son embouchure (5 km) et son plus long diamètre (13 km) la classifie comme une baie renfermée. À 2.3 m et 3.7 m de marnage pour les marées moyennes et les grandes marées (Procéan, 1999), la BSI serait considérée comme un estuaire mésotidal par Dyer (1973). À l'intérieur du transect T1 (figure 2) la baie contient environ 1.1 km^3 d'eau et s'étend sur 100 km^2. De cette superficie, les profondeurs inférieures et supérieures à 30 m représentent respectivement 58% et 11%. Le reste représente la zone in-
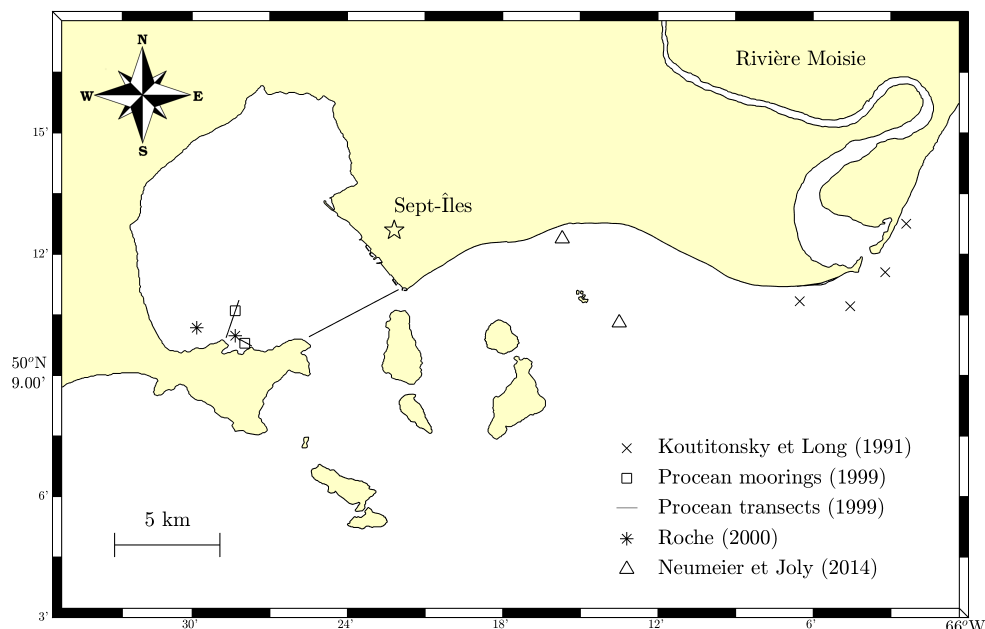
FIGURE 1: Géographie des mesures courantologiques effectuées dans la BSI par des études précédentes. Les symboles marquent des mouillages et les lignes des transects d'ADCP en route.

tertidale le long des berges. La profondeur maximale à l'embouchure est de 72 m et vers l'aval, la profondeur augmente parfois au-delà de 100 m pour former les passages entre les six îles et la presqu'île qui donnent à la baie son nom. Les rivières Hall, aux Foins, du Poste et des Rapides se déversent dans la baie en provenance d'un bassin versant dont la superficie est 788 km^2. Elles apportent 22 m^3 s^{-1} d'eau douce en moyenne annuellement (Procéan, 1999).

Il existe certaines études décrivant des mesures hydrodynamiques dans la BSI, mais leur couverture spatiale ou temporelle est souvent très locale. La répartition géographique des mesures courantologiques récoltées pour ces études est présentée à la Figure 1. Une dérive

littorale vers l'ouest est proposée par Hein et al. (1993) pour expliquer l'évolution moderne des dépôts de métaux lourds sur le delta de la rivière Moisie, à l'est de Sept-Îles. Des courantomètres ont été placés à l'embouchure de la rivière Moisie par Koutitonsky and Long (1991) qui ont enregistré des vitesses instantanées de l'ordre de 20 cm s^{-1}, globalement orientées le long des berges vers le sud-ouest. Ils ont aussi enregistré des vitesses allant jusqu'à 1.5 m s^{-1} durant les tempêtes et noté la corrélation de ces vitesses avec la hauteur de la houle. Deux courantomètres ont été mouillés par Neumeier and Joly (2014) à environ 10 km à l'est de la BSI de 2010 à 2014. L'un était près de la côte à une profondeur de 4.4 m alors que le second était à 4.5 km de la côte à 28 m de profondeur. Il ont trouvé que les courants dans cette zone s'écoulaient généralement le long des côtes et changeaient de direction selon les marées, mais sont dominants vers l'ouest lorsque moyennés sur 4 ans à l'exception des courants de surface au mouillage profond qui sont dominants vers l'est. À l'intérieur de la baie, Roche (1991) (consulté dans Belles-Isles et al. 2003) décrivent des courants qui longent les berges, mais dont la direction change avec les marées près de la ville de Sept-Îles. L'étude la plus exhaustive à ce jour a été menée par Procéan (1999) qui emploie deux mouillages équipés de courantomètres acoustiques (ADCP) placés dans la portion sud de la baie, ainsi que des transects d'ADCP en route répétés pendant un ou deux cycles de marée à trois endroits différents. Leur mouillage le plus profond (S1) signale des courants plus forts en profondeur (0-35 cm s^{-1}) qu'à mi-profondeur (0-17 cm s^{-1}) et dirigés vers 290°ou 135°, selon les marées. Ils détaillent les courants à l'embouchure à marée haute, marée basse, au jusant et au flot tel que mesurés par leur ADCP en route. En surface, ils trouvent des vitesses vers l'amont à toutes les phases de marée sauf le jusant. Les vitesses maximales (~42 cm s^{-1}) y sont mesurées en période de flot. Au jusant, les courants de surface sont mesurés vers l'aval à l'exception d'un courant vers l'amont mesuré près de Pointe à la Marmite. En profondeur, ils mesurent des courants plus faibles (< 20 cm s^{-1}) et plus spatialement variables qui s'écoulent vers l'aval. Des courants encore plus faibles (< 10 cm s^{-1}) sont toutefois mesurés vers l'amont pour ces profondeurs à plusieurs phases de marée. Les transects répétés à l'intérieur de la baie ont montré jusqu'à quatre couches de courants cisaillés que Roche (2000) interprète comme des cellules verti-

cales forcées par le vent telles qu'on en retrouve dans les modèles physiques de lacs stratifiés (Hutter et al., 2011). Roche (2000) ont aussi mouillé des courantomètres dans la portion sud de la BSI pendant 66 jours. Ils ont mesuré des courants allant jusqu'à 40 cm s^{-1} et longeant principalement la côte. Une analyse de vecteur progressif pour ces données montre une vitesse résiduelle vers l'est dans cette région. Leur rapport présente également des profils de conductivité, température et profondeur (CTD) provenant de plusieurs endroits dans la BSI montrant une stratification à deux couches dont celle de surface (0-15 m) était caractérisée par des températures et salinités de ~10°C et ~30 PSU, alors que ~4°C et ~31 PSU sont mesurés en couche de fond le 6 août 1999. À partir de ces données, ils proposent un modèle conceptuel pour la circulation dans la BSI dont la forme est représentée par un réservoir circulaire avec une entrée d'eau orientée vers le nord connectée à son extrémité est. Ils considèrent que la circulation est cyclonique lorsque l'eau entre dans le réservoir et anti-cyclonique convergente vers l'entrée lorsque l'eau en est retirée. Aucune mesure, simulation ou référence n'est toutefois présentée en appui à ces affirmations. Si leurs données de mouillage et leur modèle conceptuel sont en accord, les données sont très localisées. Leurs mouillages étaient à 1 km de séparation le long de l'isobath 10 m, à environ 0.5 km de la berge sud. Aucune donnée n'est présentée qui permet d'évaluer la validité du modèle conceptuel ailleurs dans la BSI.

Méthodologie

La visite de 21 stations réparties dans la baie et l'archipel pour y récolter des profils de température, salinité et courants, répétée à 5 reprises au cours de l'été 2017 (tableau 1) constituait le coeur de l'échantillonnage de ce projet de recherche. Le transect T1 (figure 2) à l'embouchure de la baie a aussi été choisi pour explorer la variabilité tidale de la BSI. Des passages répétés ont été réalisés en le longeant durant un cycle de marée semi-diurne (12 h), récoltant des profils de courantomètre acoustique à effet doppler (ADCP) en continu et des profils CTD lors d'un passage sur trois. Des bouées dérivantes munies de balises GPS ont aussi été déployées lors des transits afin de récolter de l'information sur les courants de

surface. Toutes les données de 2017 ont été collectées à bord du navire de pêche au crabe le *Yvan-Raymond*, à l'exception d'un déploiement de bouées le 26 septembre effectué à partir d'un plus petit navire, le *Monica*. Les mesures d'ADCP en route collectées en mai 2018 le long des transects T1 et T2 (voir figure 2) ont été collectées à bord du navire *F. J. Saucier* appartenant au Centre interdisciplinaire de recherche en cartographie des océans (CIDCO).

Dates (dd/mm/yyyy)	Stations CTD	Stations ADCP	Bouées	ADCP en route	CTD T1
04-06/05/2017	×	×	×		
21-22/05/2017	×				
06-07/06/2017	×	×	×		
19-23/06/2017	×	×	×	×	×
24-26/09/2017	×	×	×	×	×
15-18/05/2018			×	×	×

TABLE 1: Sommaire des dates et opérations de collecte de données.

Une pleine compréhension de l'hydrodynamique d'un bassin comme la BSI est difficile à atteindre sans avoir recours à la modélisation. Les travaux présentés ici visent néanmoins à en produire une description aussi détaillée que le permettent les observation recueillies. À cette fin, un portrait des conditions de vent (section 1.4.2), des marées (section 1.4.1) et du débit des tributaires a d'abord été dressé à l'aide de données obtenues d'Environnement et changement climatique Canada (ECCC), du Service hydrographique du Canada (SHC) et du Centre d'expertise hydrique du Québec (CEHQ). Un large éventail d'analyses intégrant ces données contextuelles avec les données nouvellement acquises ont ensuite été effectuées pour en dégager les tendances tidales et saisonnières décrites à la section 1.4.3, ainsi que les tendances spatiales décrites à la section 1.4.4. Ces résultats ont permis de proposer une compréhension préliminaire de la circulation dans la BSI synthétisée aux sections 1.5.4 et 1.5.5. Ils ont aussi permis d'avancer des recommandations d'expériences à conduire advenant qu'une étude de modélisation numérique soit réalisée.

ARTICLE I

HYDRODYNAMICS OF THE BAY OF SEPT-ÎLES

1.1 Abstract

Seasonal and tidal variability of temperature, salinity, and currents were measured in the bay of Sept-Îles from spring to fall 2017, and in spring 2018. Surface drifters and ADCP profilers were deployed to measure current velocities and CTD profiles were recorded regularly at 21 stations spread out across the bay and archipelago. Repeated passages along a transect at the bay mouth were conducted during 12 hours with an underway ADCP. During these transects, regular stops were made for CTD profiling. Seasonal disturbance of stratification was strongest in early June and was mostly felt in the top 20 meters. Tidally-averaged currents were out-flowing near the surface (0-5 m) and generally in-flowing in deeper waters (15-50 m). A seaward current was measured near Pointe à la Marmite throughout the tidal cycle and also appears in drifter data. Surface drifter speeds average to 17.4 cm s^{-1} but reached up to 86.6 cm s^{-1}. Drifter heading was 24±39° west of wind direction on average and they shoaled on beaches opposing dominant wind directions (NNW and ESE) in 22/46 cases. A bay scale anti-cyclonic current was measured at rising tide and surface circulation during ebb was cyclonic on average. Bulk residence time for water in the BSI is scaled to 2-12 days. The internal Rossby radius is scaled to $L_D = 2.8$ and $L_D = 6.8$ during low and high stratification, suggesting influence of earth's rotation on hydrodynamics can not be neglected. Criticism of the existing conceptual model for circulation in the BSI, and a starting point for a new model are given.

1.2 Introduction

Objective evaluation of the health of an ecosystem can prove to be a complex task especially in the presence of a richly diverse biota, such as is often found in bay environments (Greenlaw et al., 2011). In an effort to monitor the global health state of ecosystems using a finite set of parameters, ecological indicators have developed notably in Europe (Birk et al., 2012), and in various places (Halpern et al., 2008), designed for local application.

The Ocean Health Index (OHI) developed by Halpern et al. (2012) exemplifies this method. To produce an ecosystem's score according to its framework, response of an ecosystem to anthropogenic, biological and climatic stress factors is used to predict its future state. Comparison of this future state with a reference healthy state determines the ecosystem's health score. However, it is a known caveat that ecological indicators are often unreliable outside the ecosystem for which they were designed (Gillett et al., 2015).

In the context of growing anthropic presence at sub-arctic and arctic latitudes, there is a corresponding growing need for the development of tools to help managers make sustainable and science-based decisions. To answer this need, a multidisciplinary study was conducted by the Canadian Healthy Oceans Network (CHONe) strategic partnership in collaboration with the Nordic institute of research in environment and health in the workplace (INREST) aiming at designing ecosystemic health indicators tailored to the bay of Sept-Îles (BSI, Figure 2). A challenge to this goal is the lack of key information, such as knowledge of hydrodynamic conditions and their variability.

Strongly industrialized and subject to international maritime traffic, the BSI finds itself near other ecosystems (Baie St. Marguerite, Baie Moisie) which are subject to little or no anthrophogenic influence making this region a suitable location to study the effects of anthropogenic stress on benthic and pelagic sub-arctic communities.
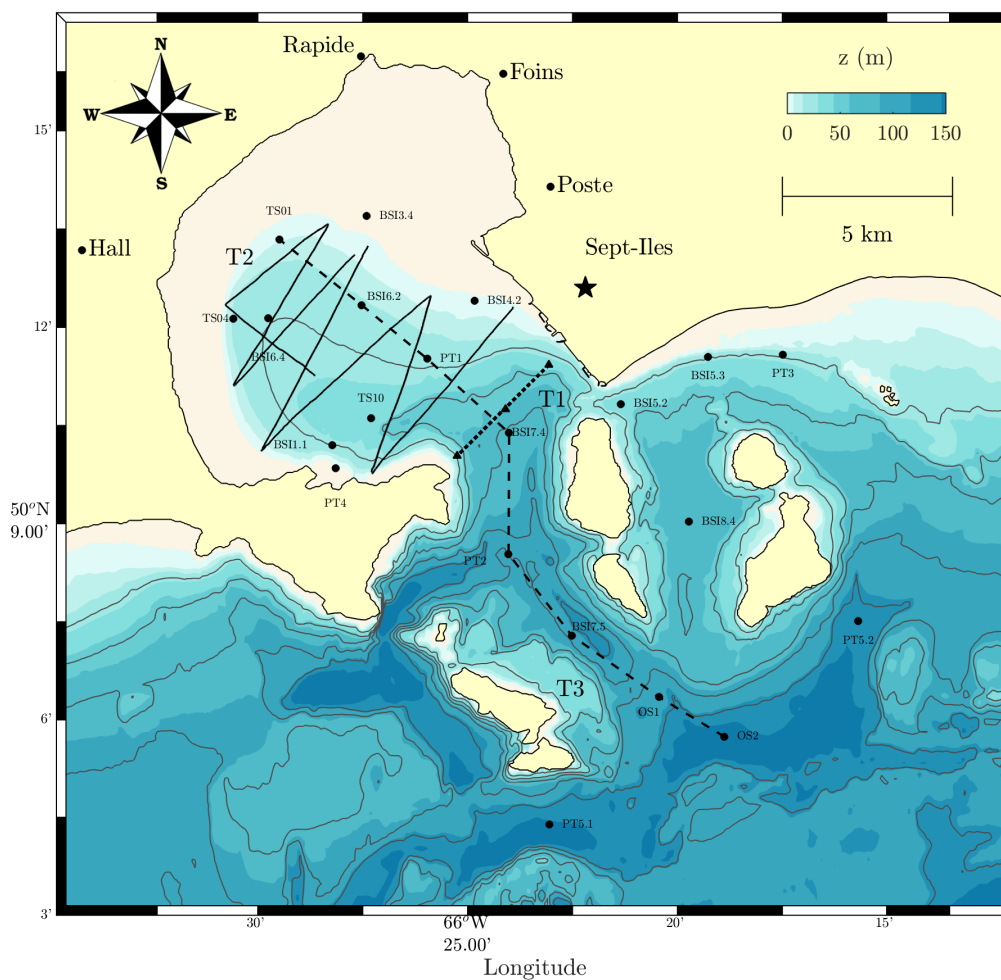
Figure 2: Regular sampling stations (●) and transects. Stations marked by ▲ only sampled during 12 h repeated transects. The locations on land are the bridges from which the rivers were sampled. T1 (dotted) and T2 (solid) correspond to underway ADCP transects. T3 (dashed) is the main CTD transect. Bathymetric contours are 5 meters apart. Solid contours mark 25 m intervals.

The BSI (Figure 1) is located at 50° N, in the north-west portion of the Gulf of St. Lawrence (GSL). Comparing the lengths of its opening (5 km) to its largest diameter (13 km) classifies it as an enclosed bay (Healy and Harada, 1991). It provides a natural harbor of approximately 100 km². It is surrounded by tidal flats which are wider to the north (3 km) than to the west

(1 km) (Procéan, 1999). Between the 0 m isobath and transect line T1 (Figure 2), the mean depth is 16.5 m. The BSI deepens towards its mouth reaching a maximum on T1 of 71.3 m. Outside the bay, the ocean floor drops steeply, sometimes deeper than 100 m, to form the passages between a seven island archipelago.

There exist a limited number of studies describing hydrodynamic measurements in BSI, but they are often focused on local areas of the BSI and are not designed to provide understanding of the whole system. Figure 1 shows where current measurements have been conducted prior to this study. Westward coastal drift was proposed by Hein et al. (1993) to explain the modern evolution of heavy metal deposit concentrations on the Moisie delta, east of Sept-Îles. Three current meters were moored at 8 m depth near the Moisie river mouth by Koutitonsky and Long (1991) which recorded instantaneous velocities on the order of 20 cm s^{-1}. Averaged over several weeks, these velocities were towards 229° at 2.0 cm s^{-1} supporting the hypothesis of a westward current along the shore. They also recorded maximum water velocities of 1.5 m s^{-1} during storms and noted correlation between current and swell height. Two upward-looking current meters were moored by Neumeier and Joly (2014) approximately 10 km east of the BSI mouth from 2010 to 2014. One was near the shore in water 4.4 m deep while the other was 4.5 km offshore in water 28 m deep. They found that currents in this area were generally along shore and reversed with tides, but were dominantly westward when averaged over 4 years with the exception of surface currents from the deeper mooring which were dominantly eastward. Inside the bay, Roche 1991 (consulted in Belles-Isles et al. 2003), describe long shore current direction alternating with tide near Sept-Îles. The most exhaustive study yet was led by Procéan (1999), relying on two moorings equipped with ADCPs and placed in the southern portion of the bay, as well as repeated underway ADCP transects during one or two tidal cycles. Their deeper mooring (S1) reports currents stronger in depth (0 − 35 cm s^{-1}) than at mid-depth (0 − 17 cm s^{-1}) and directed towards approximately 290° or 135°. They detail current speeds across the BSI's entrance at high tide, low tide, ebb, and flood, as measured using the underway ADCP and found inward flow near the surface at all phases but ebb, with strongest velocities (∼ 42 cm s^{-1}) during flood. At ebb,

surface currents flow outward with the exception of inward flow developing near the western coast. At depth, they measured weaker (< 20 cm s^{-1}) and more spatially variable currents which generally flow out, but yet weaker (< 10 cm s^{-1}) inflowing currents are also measured towards the center of the transect at many tidal phases. The ADCP transects conducted cross-shore inside the bay revealed up to 4 layers of sheared currents. Roche (2000) interprets this layer structure as wind driven cells found in simplified models of stratified lake physics as described in Hutter et al. (2011). This model states that when wind forces downwind current at the surface of a closed basin, water accumulates at the leeward shore. The resulting pressure gradient generates upwind current at depth. When the basin is stratified, this circulation happens in the surface layer. Upwind current at the bottom of the top layer, near $z = 15$ m in the case of the Procéan (1999) measurements, then forces a counter rotating current cell in the bottom layer through similar dynamics. Roche (2000) also placed two current meters in the southern portion of the bay for 66 days. They measured mainly along shore currents in the range $0 - 40$ cm s^{-1}, and progressive vector analysis shows net current is towards the east in this region. Further, this report presents CTD profiles from four stations which show two layer stratification across the BSI, with the top layer at $T \sim 10°$C and $S \sim 30$ PSU, and bottom layer at $T \sim 4°$C and $S =\sim 31$ PSU, on August 6, 1999. They propose a conceptual model for circulation in the BSI consisting of a cylindrical tank with a water input pointing north and connected to the eastern side. They state that this system results in cyclonic flow as water is input, whereas flow is anti-cyclonic and converges towards the entrance when water is removed. No measurements, simulations or references are presented however to support these hypotheses. While their mooring data and conceptual model agree, their data is very localized. The moorings were 1 km apart along the 10 m isobath, roughly 0.5 km from the bay's southern shore. No data is presented that can evaluate the validity of their conceptual model elsewhere inside the bay. This model will be discussed in light of data collected during this study in section 1.5, and recommendations towards an updated model will be made.

The objective of this study is to provide information about spatial and temporal variability of hydrodynamic conditions in the BSI through collection and analysis of field measure-

ments. Section 1.3 of this paper describes the methods used, with subsections 1.3.1, 1.3.2, and 1.3.3 focusing respectively on field sampling, third party data sets, and data processing. Section 1.4 presents the results of this study. It is divided into subsections describing forcing conditions of wind and tide on the BSI (1.4.2, and 1.4.1), the temporal variability (1.4.3), and the spatial variability (1.4.4). Results are integrated and discussed in section 1.5.

1.3 Datasets and Methodology

1.3.1 Sampling

To assess spatial and seasonal variability of hydrodynamic conditions a set of 21 stations shown on Figure 2 were visited 5 times over the summer of 2017 (see Table 2 for dates and operations). Transect T1 (Figure 2) was chosen to explore tidal variability. Repeated passages were conducted along this line during a semi-diurnal tidal cycle (12 h) while collecting acoustic doppler current profiler (ADCP) data continuously, and CTD profiles at three stations during one passage out of three. All sampling from 2017 was collected from the *Yvan-Raymond* crab fishing vessel with the exception of a drifter deployment on September 26 conducted from the smaller fishing vessel, the *Monica*. The May 2018 underway ADCP data along transects T1 and T2 (Figure 2) was collected on board the Interdisciplinay center for the development of ocean mapping (CIDCO) hydrological survey boat *F. J. Saucier*.

A Seabird model 19plus CTD probe equiped with an additionnal model 43 dissolved oxygen sensor and a fluorescence sensor was used. Continuous profiles were thus obtained for salinity, temperature, dissolved oxygen, fluorescence and turbidity. Weather permitting, profiles were collected once at all stations for every presence of the team on site. During the May 2018 campaign, CTD profiles along T1 were instead collected using a YSI Cast Away portable CTD. Sampling rates for both probes used was 4 Hz. All CTD profiles were averaged into 1 m vertical bins.

Dates (dd/mm/yyyy)	CTD stations	ADCP stations	Drifters	Towed ADCP	T1 CTD
04-06/05/2017	×	×	×		
21-22/05/2017	×				
06-07/06/2017	×	×	×		
19-23/06/2017	×	×	×	×	×
24-26/09/2017	×	×	×	×	×
15-18/05/2018			×	×	×

Table 2: Summary of sampling dates and data sets collected.

Current profiles were collected using Teledyne RDI Sentinel V 500 kHz ADCPs. One was lowered to ~1 m beside the boat while other measurements were conducted and the other was fixed on a Biosonics BioFin aluminum towing body and towed at a speed of approximately 2 m s^{-1}. Both ADCP's ping frequencies were set to 2 Hz. The stationary measurements used 1 m vertical bins yielding a range of 100 m in depth. This ADCP was lowered about 1 m beneath surface for stability, so added to the blank distance of 1.6 m, this places the first bin's center at roughly 3 m. Since the transects using the towed ADCP were usually carried out in relatively shallow water, a resolution of 0.5 m between bins was chosen yielding a 50 m range in depth. The towing body's mean depth was 0.9 m and the center of the first bin was 2.6 m deep. To correct for the boat's movement, a 5 second interval position log has been kept using a Garmin GPS device. Teledyne RDI documentation for the Sentinel V ADCP specifies that its velocity accuracy is 0.3% of the water velocity $\pm$ 0.3 cm s^{-1}. For profiling velocities smaller than 50 cm s^{-1}, accuracy can be expected to be better than 0.5 cm s^{-1}

Firmware of the towed ADCP was upgraded from Self-contained version 47.19.00.24 to Real-Time version 66.02.00.05 prior to sampling conducted in May 2018. This allowed the use of bottom-tracking, absent from the other ADCP data sets, but imposed a lower frequency of 0.5 Hz. Acquisition was performed using the Teledyne RD VMdas platform with position taken from the hand held Garmin device in some cases and the ship's Hydrinks IXBlue inertial central for others. Underway ADCP velocities along both T1 and T2 were smoothed with a 63

ping horizontal moving average and gridded at a resolution approximately equivalent to the distance travelled by the boat in the corresponding time (252 m). Due to conditions inherent to the BSI, it was only possible to gather ADCP data reliably in the top 30 m, as was also noted by Procéan (1999).

The surface drifters employed are home made, consisting of a wooden base approximately 30 cm in diameter, on which is fixed a Spot Trace GPS device. When in motion, the Spot signals its position via satellite every ten minutes and the data is accessible in real time. To ensure the emitter remains above surface, the opposite side of the base is attached with a 0.9 kg training weight, hanging from a steel wire approximately 0.5 m deep. The drifters were usually deployed on an opportunistic basis, often during transit between stations. One scheduled deployment was conducted in September 2017 where a grid of 11 drifters were spread as quickly as possible (2 h) over the area of the bay contained by the 5-m isobath. Drifters were also purposefully deployed near the mouths of rivers Poste, aux Foins and Rapides. Deployments were more concentrated inside the bay area since chances of recovery were higher in these conditions.

Though 24 drifters were used, through recovery and redeployment, 46 continuous drifts were collected providing 560 hours of drift data. Surface currents were thus measured several times during the season and under various different wind conditions. Data acquired during flood tide makes up 57.3% of the received positions hinting a possible over representation of this phase. Drifter tracks from 2003 sampled by the Department of Fisheries and Oceans Canada (DFO) in the BSI complement our data set with 52 additional drift hours (D. Lefaivre, personal communication).

Positions where drifters remained persistently at low speeds ($|\mathbf{u}| < 5$ cm s^{-1}), and low depth ($z < 2$ m) with tide accounted for, were considered shoaled and were removed from analysis. The drifts were then interpolated on a regular 10 minute time grid.

1.3.2 Third party data

Previous studies of wind statistics exist for the BSI which use long climatologies of wind measured at the nearby airport (Procéan, 1999; Baird, 2005). Using wind model solutions instead allows interpretation of data over the bay. Hourly wind data from the Canadian Meteorological Center's high resolution deterministic predictive system (HRDPS) (Milbrandt et al., 2016) was used in this study. The statistics computed use wind 10 m above water from 34 grid points at 2.5 km spatial resolution. Chosen points are over water, and found between longitudes 66°21′ and 66°33′W, and latitudes 50°9.00′ and 50°16.38′N. Data considered for summer months starts on April 1, 2017 and ends on October 31, 2017, while winter data is from November 1, 2017 to March 31, 2018.

Sea level data (46 years) archived by Canadian Hydrographic Service was used for tide related analyses. Collected data was also analysed in conjuction with coast line data from the United States Geological Survey (USGS), Moisie River and historical Rapides River (1947-1983) discharge data from the centre d'expertise hydrique du Québec (CEHQ), and St. Lawrence discharge at Quebec city (RIVSUM) (Bourgault et al., 1999; Galbraith et al., 2017) courtesy of DFO. The interpolated bathymetry is a product created by Simon Senneville (ISMER, pers. comm.) with data from the Canadian Hydrographic Service (CHS) in accordance with the CHS direct user licence no° 2013-0304-1260-O.

1.3.3 Processing

It is useful to define a frame of reference aligned with the best fitted straight line through the GPS data from 12 hours of repeated transects across the bay's entrance (transect T1). Coordinate x_c points along the mean transect towards Sept-Îles, holding origin near Pointe à la Marmite, where this line meets the shore. Coordinate x_a is normal to x_c and points downstream (Figure 3). Repeated measurements along a transect has shown to allow for non synoptic reconstruction of the measures over the whole transect through repeated 1D

interpolation (Matte et al., 2014). This is applied to the ADCP, and CTD data collected on transect T1.

Currents and CTD profiles are projected onto the mean transect line x_c, computed from linear regression of GPS data from the 12 hours of measurement. They are then gridded in 1D along x_c at a resolution of 252 m, chosen to match the ADCP horizontal averaging window size, prior to time interpolation. CTD cast positions along x_c were near $x_c = 0.56$, 2.47, and 4.22 km.
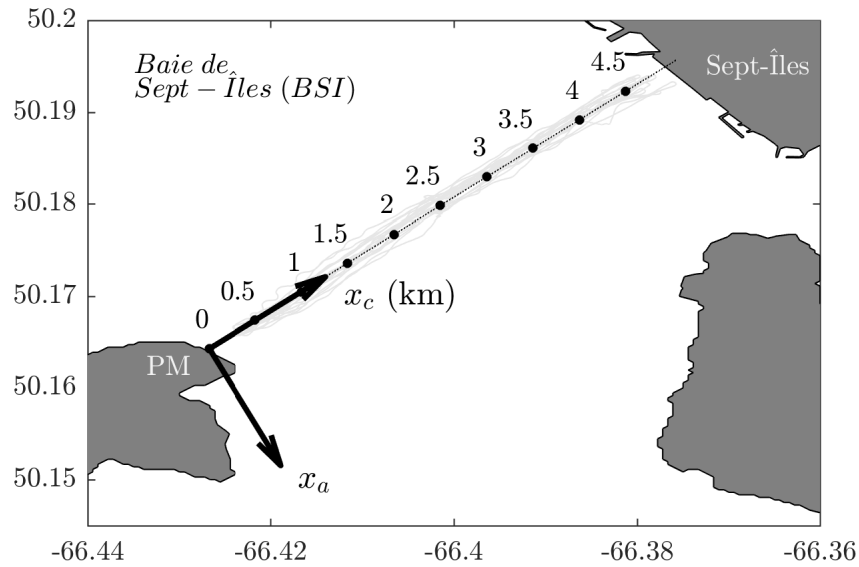
Figure 3: Definition of coordinates x_c and x_a along transect T1.

Since the bay has only one opening to the GSL, the time derivative of integrated flow $\mathbf{u}$ through section T1 is balanced by the corresponding change in water volume inwards of T1. This is summarized by the mass conservation equation, that is

$$\frac{\partial V}{\partial t} + \oint_S \mathbf{u} \cdot \partial \mathbf{S} = 0 \tag{1.1}$$

where V is the volume of water contained in the BSI inward of T1, and S the surface contain-

ing volume V. Let now s be the portion of S representing the surface of the bay, $\bar{s}$ the average bay surface during a time interval ∂t. The rate of change of the bay volume is expressed as

$$\frac{\partial V}{\partial t} = \bar{s}\,\frac{\partial h}{\partial t}. \tag{1.2}$$

Assuming the river inflow is negligible as compared to flow through T1, the closed boundary conditions at land and at the sea surface then imply $\mathbf{u} \cdot \partial \mathbf{S}$ will be zero everywhere on S except on section T1. Taking the z axis to be positive downward, we can therefore rewrite the surface integral of equation 1.1 as an integral over cross section T1, and integrate it over a time period Δt such that

$$-\,\bar{s}\int_0^{\Delta t}\frac{\partial h}{\partial t}\partial t + \int_0^{\Delta t}\int_0^{l}\int_0^{D(x_c)} u_\perp(x_c, z)\,\partial z\partial x_c\partial t = 0 \tag{1.3}$$

where $u_\perp$ is the cross transect component of water velocity, defined positive downstream, l is the horizontal length of T1 from shore to shore, $D(x_c)$ is the position-dependent depth along T1, and $\partial \mathbf{S}$ has become $\partial z\partial x_c$. $u_\perp$ can be further decomposed as

$$u_\perp = u_a + u_m \tag{1.4}$$

where u_a is velocity available from ADCP data, and u_m the velocity missing from ADCP data. Supposing now that the interval Δt is small enough that water velocity remains constant, and substituting equation 1.4 into 1.3 we have

$$\bar{s}\Delta h = \Delta t \int_0^{l}\int_0^{D(x_c)} u_a\,\partial z\partial x_c + \Delta t \int_0^{l}\int_0^{D(x_c)} u_m\,\partial z\partial x_c. \tag{1.5}$$

where Δh is the change in water level after Δt. Now let n be the amount of ADCP measurements available at a given time on T1, γ the area of which ADCP measurements are representative, determined by vertical bin size and horizontal averaging window size, and α the total area of section T1. An average outward velocity $\bar{u}_a$, may be defined across the whole

unmeasured area as

$$\bar{u}_a = \frac{1}{\alpha - n\gamma} \int_0^l \int_0^{D(x_c)} u_m \, \partial z \partial x_c.$$ (1.6)

Substituting equation 1.6 into 1.5 and rearranging we obtain

$$\bar{u}_a = \frac{1}{\alpha - n\gamma} \left[\bar{s} \frac{\Delta h}{\Delta t} - \int_0^l \int_0^{D(x_c)} u_a \, \partial z \partial x_c \right].$$ (1.7)

Equation 1.7 can then be discretised and time stepped through the tidal cycle where current velocities are known to obtain

$$\bar{u}_a^m = \frac{1}{\alpha - n^m\gamma} \left[\frac{\bar{s}^m(z^m - z^{m-1})}{t^m - t^{m-1}} - \sum_{i=1}^{n^m} u_i^m \gamma \right]$$ (1.8)

where $\bar{u}_a$ is computed for time step m, for which n ADCP measurements exist. Note that γ is kept constant and so is α, since it would vary at most by 5% over a tidal cycle of 2 m in range. Note also that $\bar{s}$ is constant during each time step, but varies for distinct time steps.

Since available bathymetric data did not extend to the shore line, linear interpolation was conducted between both data sets with coast set in elevation at the average of the highest seas of every month in the available time series, $z = -3.35$ m.

Extrapolation of ADCP profiles towards the surface was conducted by fitting u, and v components individually with a linear combination of the 5 first horizontal velocity modes computed from the buoyancy frequency squared profile. This implies the extrapolated speeds originate only from the baroclinic tide propagating horizontally and contain no wind contribution. The five first modes were found to explain 90±1% of variance as shown in Figure 4.

Vertical velocity mode eigenvectors (Kundu et al., 1975; Pedlosky, 1987), forming the matrix $\mathbf{W}_n$ were computed using John Klinck's *Matlab* routine dynmodes.m, which solves

$$\frac{\partial^2}{\partial z^2} \mathbf{W}_n + \lambda^2 N^2(z) \mathbf{W}_n = 0$$ (1.9)

that is appropriate for horizontally propagating internal waves under traditional and hydrostatic approximations (Gerkema and Zimmerman, 2008). Supposing the solutions

$$u = U(z)e^{i(kx-\omega t)} \quad , \quad v = V(z)e^{i(kx-\omega t)} \quad , \quad w = W(z)e^{i(kx-\omega t)} \quad , \quad p = P(z)e^{i(kx-\omega t)} \qquad (1.10)$$

for velocities and pressure, it follows from the primitive equations that

$$U = \frac{i}{k}\frac{\partial W}{\partial z} \quad , \quad V = \frac{f}{\omega k}\frac{\partial W}{\partial z} \qquad (1.11)$$

where f is the Coriolis parameter. Horizontal velocity modes can therefore be obtained by taking the z derivative of vertical velocity modes.
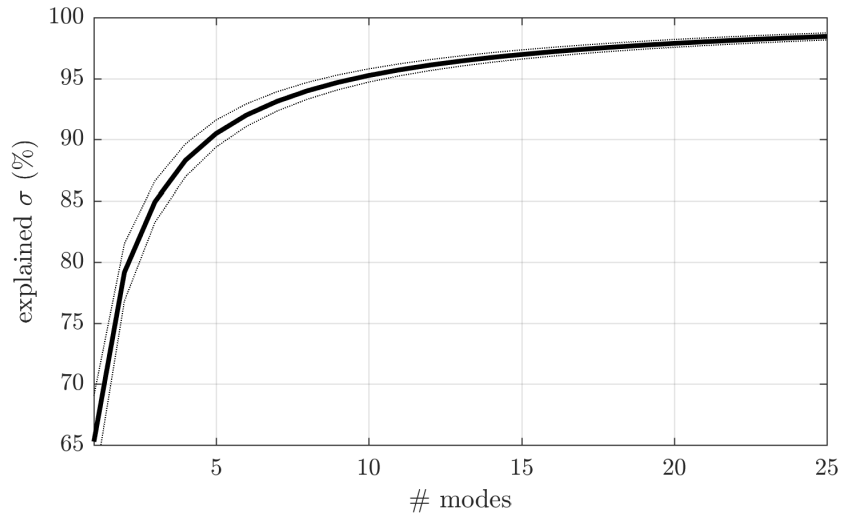
Figure 4: Percentage of ADCP profile variance explained as a function of the number of vertical modes considered. The solid line shows the average over all profiles and the envelope is standard deviation.

A genetic optimization algorithm was used to determine the modal content of ADCP profiles by finding the solution set k_n, which minimizes q defined as

$$q_u = \sum_z \Gamma(z) \left| k_0 + \sum_{n=1}^{5} k_n U_n(z) - u(z) \right| \qquad (1.12)$$

where $\Gamma(z) = z_c/z$ is a weight function used to emphasize importance of fitting the profile above z_c and avoid local minima where the rest of the profile is fit properly but the top is not, k_0 is the barotropic component of the fit, and $u(z)$ is the ADCP velocity profile smoothed with a 4 m moving average. q_v is likewise calculated and provides an independent set k_n used to fit the v component.
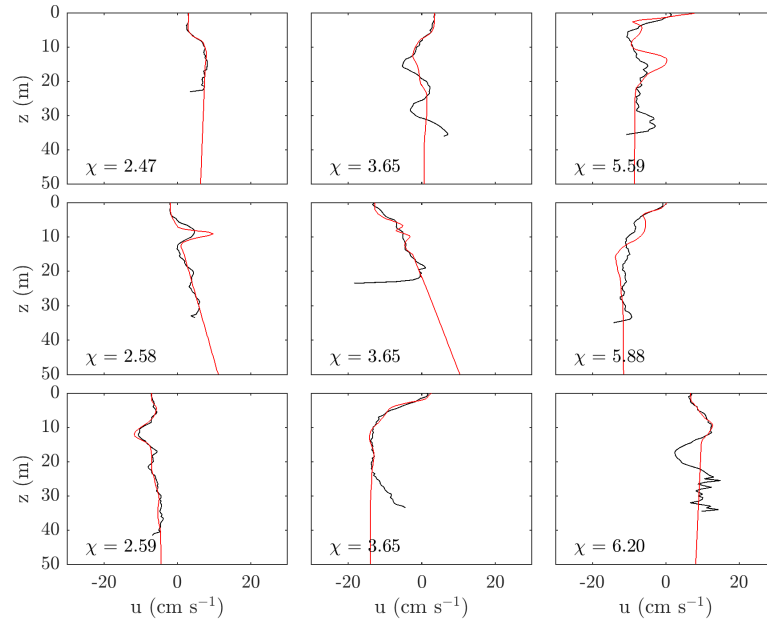
Figure 5: Eastward velocity from ADCP data (black) and adjusted current profile (red) for the three best fits (left), three average fits (center), and the three worst fits (right). Associated χ (cm s^{-1}) values are written in the bottom left.

Genetic optimization involves starting with a number of solution families (here k_n), choosing two of the most suitable and probabilistically mixing their content to produce the next generation of solution families. This process is iterated until a satisfactory solution family is produced. Here, the optimization routine was run a maximum of 1000 iterations with a population of 40 solution families and $z_c = 20$ m. After repeating this process 30 times per profile component, the best scoring solution family is used to compute the extrapolation.

Fit quality χ for one profile is defined as

$$\chi^2 = \langle (u - u')^2 + (v - v')^2 \rangle_z \qquad (1.13)$$

where primes denote fitted profiles. Averaging over all extrapolated profiles, we have $\chi = 3.71 \pm 0.69$ cm s^{-1}. Figure 5 shows fit examples for the eastward velocity component. Fits with χ below average are often associated to errors near or below z_c.

The means of normally distributed variables in this study are presented with standard deviation to the mean (SD). Statistics on circular quantities are computed using the Matlab Circular Statistics Toolbox developed by Berens (2009).

1.3.4   Problems encountered

Vessel movement influence was poorly cancelled when adding boat velocity to ADCP data without bottom tracking for all sampling conducted from the *Yvan Raymond*. This may be due to magnetic interference from the ship's engines, or irregularities in the power it supplied to the profiler. It was noticed that electric discharges could be felt while bringing the ADCP's towing body on board after sampling which is unusual with respect to other campaigns where these tools were used. In consequence, the influence of boat motion could not be removed from all station ADCP measurements, as well as from the under way measurements of May 22, and September 24, 2017. An attempt at salvaging the underway measurements is detailed in Appendix 1.

The ship's inertial central was used as a heading source for the towed ADCP during the repeated transects of May 17, 2018 at the bay mouth. During this day, sampling was conducted under weather windy enough to rock the boat steadily. It was later found that heading from the GPS position track, and heading deduced from the bottom track velocities were abnormally different. This may be explained by the towing body being frequently forced out of alignment by ship roll and heave. In this case, using the ship's heading to rotate the

velocity data from beam to earth coordinates is likely erroneous. This is fixed by calculating a heading from bottom track velocity to compute orientation of the towing body as detailed in appendix 1. The difference between ship's heading and towing body heading is then used to complete the horizontal rotation to earth coordinates.

1.4 Results

1.4.1 Harmonic analysis of tides

Forty six years of sea level data were available over the period 1972 to 2018. Harmonic analysis was performed using the Matlab package developed by Codiga (2011), and its results are shown in Table 3. Tides in BSI are largely semi-diurnal with consituents M_2 and S_2 encompassing 86.49% of tidal energy. Over the studied time series, average tidal range was $r = 1.90 \pm 0.60$ m and the largest tidal range was $r = 3.91$ m, measured on January 10, 1982. The average period between two high tides P, was 12 hours and 25 minutes.

Constituent	P (days)	A (m)	E (%)	Phase (°)
M2	0.518	0.91	79.02	183.84
S2	0.500	0.28	7.47	225.27
K1	0.997	0.21	4.27	275.44
O1	1.076	0.20	3.75	250.81
N2	0.527	0.20	3.69	158.35
K2	0.499	0.08	0.58	223.35
P1	1.003	0.07	0.45	271.19
NU2	0.526	0.04	0.12	159.90
Q1	1.120	0.03	0.12	220.49
MU2	0.536	0.03	0.11	143.59

Table 3: Name, period, amplitude, energy percentage, and Greenwich phase lag of 10 main tidal constituents, sorted by decreasing energy.

The largest and smallest ranges of every month are averaged to produce typical neap and spring tide values of $r = 0.54 \pm 0.23$ m and $r = 3.50 \pm 0.31$ m. Minimum, maximum and,

average sea level values are -0.85 m, 4.15 m, 1.55 ± 0.75 m. Average high tide and low tide sea levels are 2.58 ± 0.41 m and 0.58 ± 0.31 m. The monthly maximum sea levels average to 3.35 ± 0.18 m.

1.4.2   Wind statistics

Seasonal and yearly wind rose plots made for the BSI using the HRDPS model solutions are shown in Figure 6. The yearly average wind speed is 4.01 ± 2.46 m s^{-1} but this value is higher (4.52 ± 2.48 m s^{-1}) and lower (3.62 ± 2.34 m s^{-1}) in winter and summer, respectively. Winds below the yearly average are more common (64%) in the summer relative to winter (48%). The strongest modelled winds blow at 19.57 m s^{-1}. In the range 105° to 125°, wind speeds greater than 10 m s^{-1} happen 0.42 ± 0.10% of time, making them 5±4 times more frequent in this direction than they are on average everywhere else (0.09 ± 0.02%).

Winds mainly blow from the three general directions NNW, ESE, and SW, whose relative importance changes throughout the year. In winter, winds blowing from the NNW (300−360°) are dominant accounting for 38% of data. Winds from a similar range (300−30°) are still notably present in summer but then account 29%. Easterly winds appear in the distributions of both seasons in the range 90−130°. For this range, they account for 15% of data in the winter and are twice as frequent (28%) in the summer. Winds from the SW (200 − 240°) are only prevalent in the summer and then account for 12% of data.
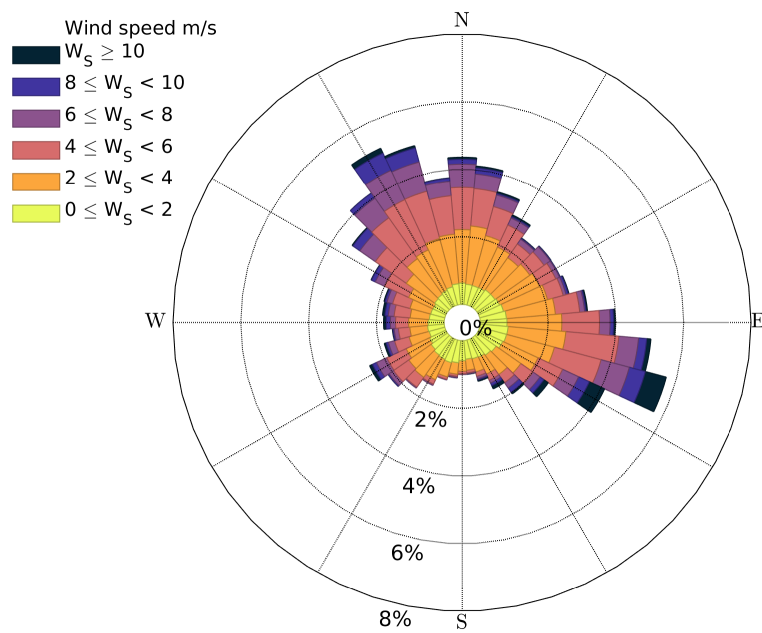
(a) Yearly winds.
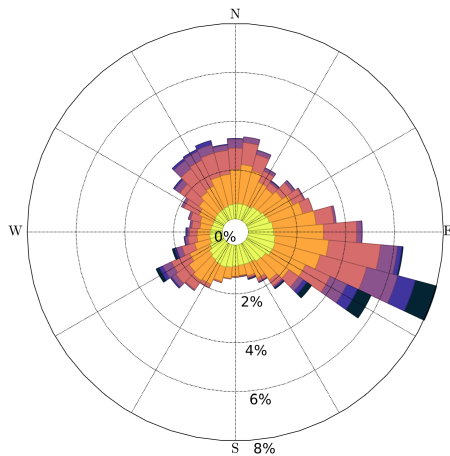
(b) Summer winds.
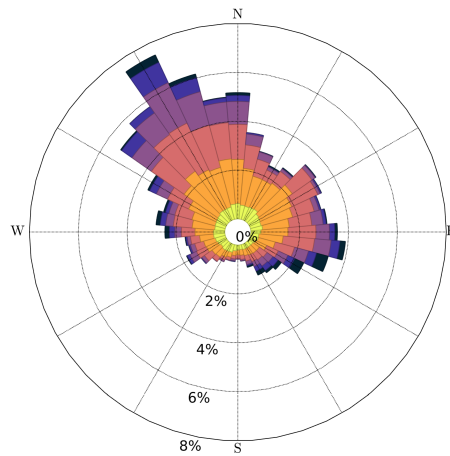
(c) Winter winds.

Figure 6: Wind provenance from the HRDPS wind model. Panel a) shows data from Febuary 2017 to Febuary 2018. Panel b) shows data from April 2017 to November 2017. Panel c) shows data from November 2017 to April 2018.

1.4.3   Temporal variability

1.4.3.1   Seasonal scale

Synoptic representation of temperature and salinity in the first 50 m of depth are shown in Figure 7 for transect T3 (see Figure 2) running from the offshore stations to the inside of the bay. Positions along T3 are given in the following as distance in kilometers from the station furthest offshore. Profiles are gathered over two consecutive days for each sampling campaign. Over the entire 2017 data set, density and salinity are highly correlated ($R = 0.99$) whereas for density and temperature $R = 0.82$. Salinity data is therefore reliably indicative of density. The maximum buoyancy frequency over all depths N^2_{max} is used in what follows as a measure of stratification. N^2_{max} values related to the transects shown in Figure 7 compose Table 4.

Minimum average stratification ($N^2_{max} = 1.6 \pm 0.79 \times 10^{-3}$ s^{-2}) is measured in early May. At this time, stratification ($N^2_{max} = 3.3 \times 10^{-3}$ s^{-2}) is 2.4 times stronger inside the bay (20 km) than on average elsewhere on the transect ($N^2_{max} = 1.4 \pm 0.41 \times 10^{-3}$ s^{-2}). Averaged over the surface five meters, water at the 20 km station is 1.7°C warmer and 0.4 PSU less salty than the other stations averaged together.

By the end of May, average stratification increases by an order of magnitude ($N^2_{max} = 2.0 \pm 2.6 \times 10^{-2}$ s^{-2}). Stratification is then maximum, comprising the two largest N^2_{max} values measured over all ($N^2_{max} = 7.8 \times 10^{-2}$ s^{-2} and $N^2_{max} = 3.7 \times 10^{-2}$ s^{-2}) interspersed with values often an order of magnitude smaller, see Table 4. Opposite to early May, stratification is now stronger outside the bay ($0 - 15$ km) where on average $N^2_{max} = 2.9 \pm 3.0 \times 10^{-2}$ s^{-2} relative to inside the bay ($15 - 20$ km) where $N^2_{max} = 4.7 \pm 2.1 \times 10^{-3}$ s^{-2}. The horizontal salinity difference is stronger with water between 15 and 20 km saltier than water in the $0 - 15$ km range by 4.8 PSU. The temperature difference for the same regions is comparable to early May in magnitude (1.6°C) but opposite in direction.

(dd/mm) / (km)	0.00	2.29	4.71	7.86	11.50	15.00	17.12	20.22
05/05	1.8	1.9	1.1	1.4	1.3	0.69	1.5	3.3
22/05	78	8	11	11	37	3	4.1	7
07/06	23	30	17	25	25	22	30	25
24/09	6.5	5.8	3.9	2.8	5	4.9	14	31

Table 4: N_{max}^2 (10^{-3} s^{-2}) for the profiles along T3 at different times of the season. Columns indicate distance from the station furthest offshore.

The strongest stratification averaged across all stations is reached in early June with $N_{\mathrm{max}}^2 = 2.5 \pm 0.4 \times 10^{-2}$ s^{-2}. Stratification is also more horizontally homogenous as is reflected by the decreased standard deviation. The largest surface temperature and salinity gradients are now further inside the bay between 17 and 20 km. The water at 20 km is colder and saltier than the rest of the stations averaged together by 3.0°C and 3.5 PSU.

The September measurements resemble those in early May. Stratification at 20 km is 5 times stronger ($N_{\mathrm{max}}^2 = 3.1 \times 10^{-2}$ s^{-2}) than the rest of the stations averaged ($N_{\mathrm{max}}^2 = 6.2 \pm 3.7 \times 10^{-3}$ s^{-2}). Average stratification decreases to $N_{\mathrm{max}}^2 = 9.3 \pm 9.4 \times 10^{-3}$ s^{-2}. As in early May, the least dense water is found near 20 km, where water is 1.9 PSU less salty than the rest of the stations averaged. No horizontal gradient of temperature appears in these measurements.

During summer, the GSL is a three layer stratified system (Galbraith, 2006). Characteristic temperature and salinity values are 1°C to 7°C and $S > 32.5$ PSU for the gulf bottom water (GBW), and the cold intermediate layer (CIL) is defined by summer temperatures below 1°C. According to these definitions, 42% and 3% of measurements match the properties characteristic to the CIL and GBW respectively. Seasonal evolution of the CIL's vertical structure has been detailed by Cyr et al. (2011). They show that during spring, when most of our measurements were collected the CIL's core is centered around 60 m and 50-100 m thick. The average depth of our measurements is 60 ± 30 m in the CIL, and 133 ± 15 m in the GBW. Influence of the CIL was therefore seen in BSI at depths typical of other areas in the

GSL during spring, while GBW was only measured deep in the channels or at the offshore stations.
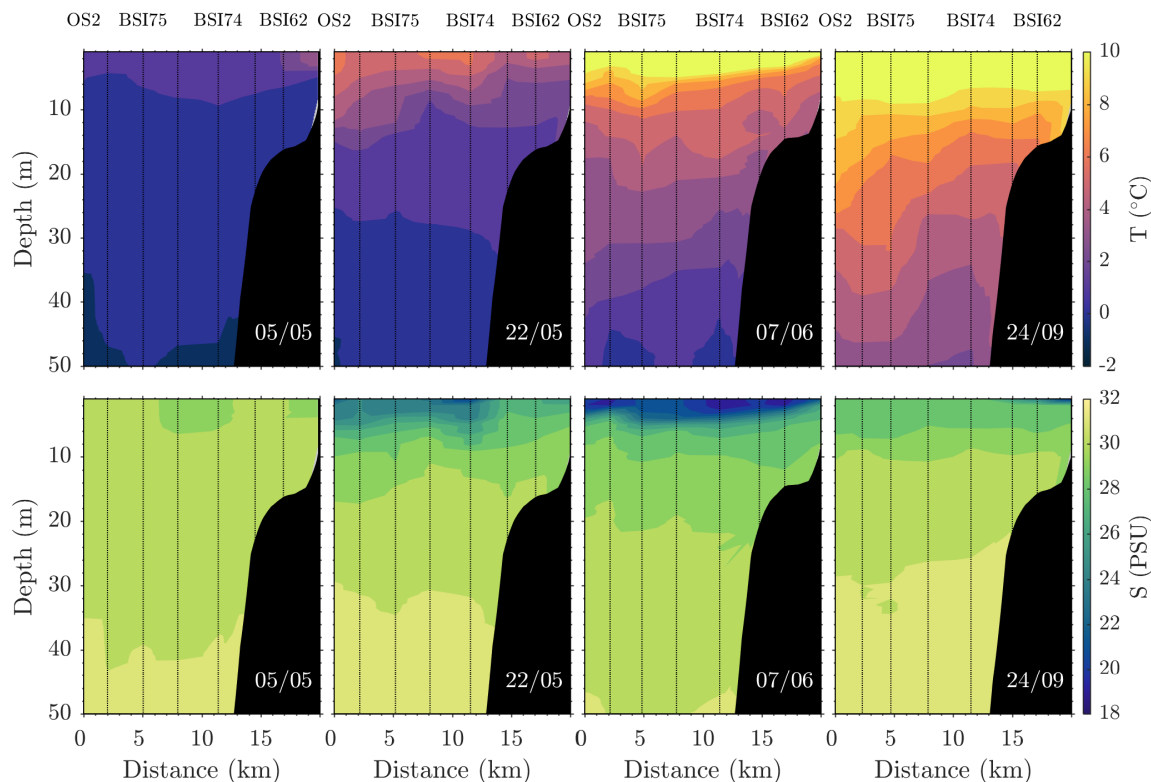
Figure 7: Seasonal change in temperature (top) and salinity (bottom) along transect T3. Distance along T3 with 0 at the offshore station is on the *x* axis. Date of sampling is written in the bottom right corner of each panel.

Table 5 lists average temperature and salinity for the top 10 meters and the 10 to 30 m layer, along with standard deviations. Salinity in both layers decreases from May to early June, then increases back to its May values by the end of September. Maximum to minimum difference is 4.9 times larger (2.7) in the surface compared to the 10 to 30 m layer (0.6). Salinity is most variable in early June for both layers but 5 times more so near the surface (SD = 3.2 PSU) than underneath (SD = 0.6 PSU). Near the surface, change in salinity is fast (~ 0.5 PSU/week) from May to June, then slower (~ 0.1 PSU/week). Underneath, the tendency is the same but rates are an order of magnitude smaller.

mm/dd	$\langle S \rangle_s$	$\langle T \rangle_s$	$\langle S \rangle_b$	$\langle T \rangle_b$
05/04	28.7 ± 2.5	2.9 ± 1.7	30.5 ± 0.4	1.1 ±0.6
05/20	27.3 ± 2.7	4.3 ± 1.2	30.3 ± 0.5	1.5 ±0.6
06/06	26.2 ± 3.1	9.3 ± 2.6	30.1 ± 0.6	3.7 ±1.6
06/22	27.3 ± 1.6	9.3 ± 2.1	30.4 ± 0.7	3.0 ±1.8
09/24	28.9 ± 1.1	10.8 ± 1.1	30.7 ± 0.3	7.0 ±1.2

Table 5: Average temperature and practical salinity shown with standard deviation for the top 10 m $\langle S, T \rangle_s$, and for the 10 to 30-m layer $\langle S, T \rangle_b$.

Average temperature increases throughout the season in the top 30 m with the exception of a small drop (top 10 m: 0.4°C , 10-20 m: 0.5°C) in late June. Near the surface, temperature rises at a rate of 0.6°C /week, and 2.1°C /week in early and late May respectively. Change is then much slower (0.1°C /week) until September. Temperatures are most variable (SD = 2.6°C) in early June near the surface but maximum standard deviation (SD = 1.8°C) is found two weeks later in the 10 to 30 m layer.

The composition of the BSI water and evolution of its surface water is summarized by the TS diagram shown on Figure 8. No salinity appears greater than ∼ 33 PSU and the bulk of the data is found at values associated with the CIL. The surface water becomes warmer and more brackish at an increasing pace from May to early June. It then continues warming and becomes saltier until September. Salinity then ressembles early May conditions with temperatures 7.96°C , and 1.06°C warmer respectively in the top 10 m, and 10 to 30 m layer.
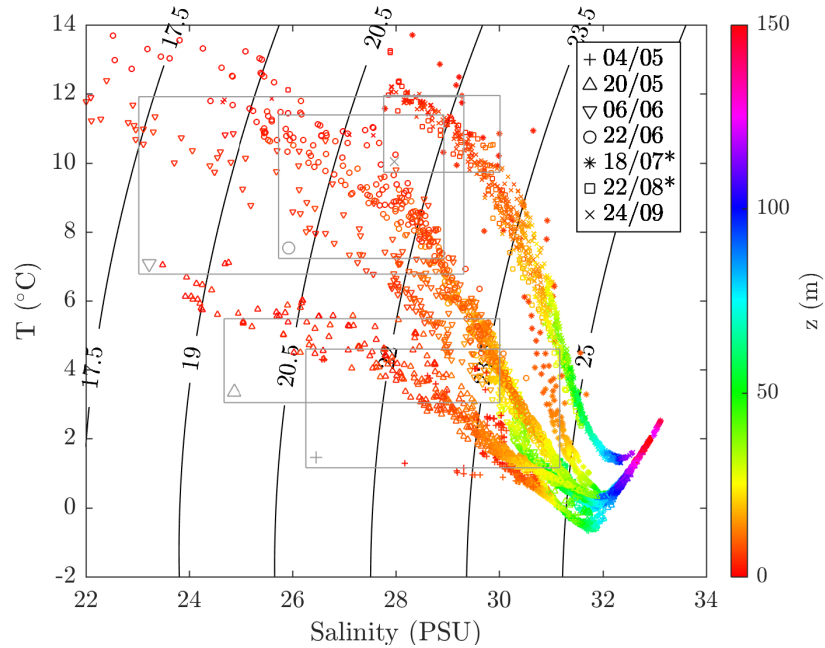
Figure 8: Temperature and salinity data and it's seasonal variability. Marker shape indicates sampling campaign and depth is shown by the color axis. '*' symbols in the legend mark sampling campaigns where only a subset of stations are visited. Salinities as low as 16.52 where measured but only in the 06/06 campaign and are not shown for clarity. Boxes are centered on the surface 10 meter mean values (see Table 5) for each campaign and are 2 standard deviations wide in both directions.

Evolution of σ_H, the density profile averaged horizontally across all stations is shown in Figure 9 for the top 30 m. The maximum standard deviation of σ_H, reflecting spatial difference between averaged profiles, is 2.17 kg m^{-3} at measured $z = 4$ m, and values decrease with depth. In the top 5 meters, σ_H variations around the seasonal mean can reach 25%. Below 5 and 22 m, variations are less than 10% and 2% respectively.
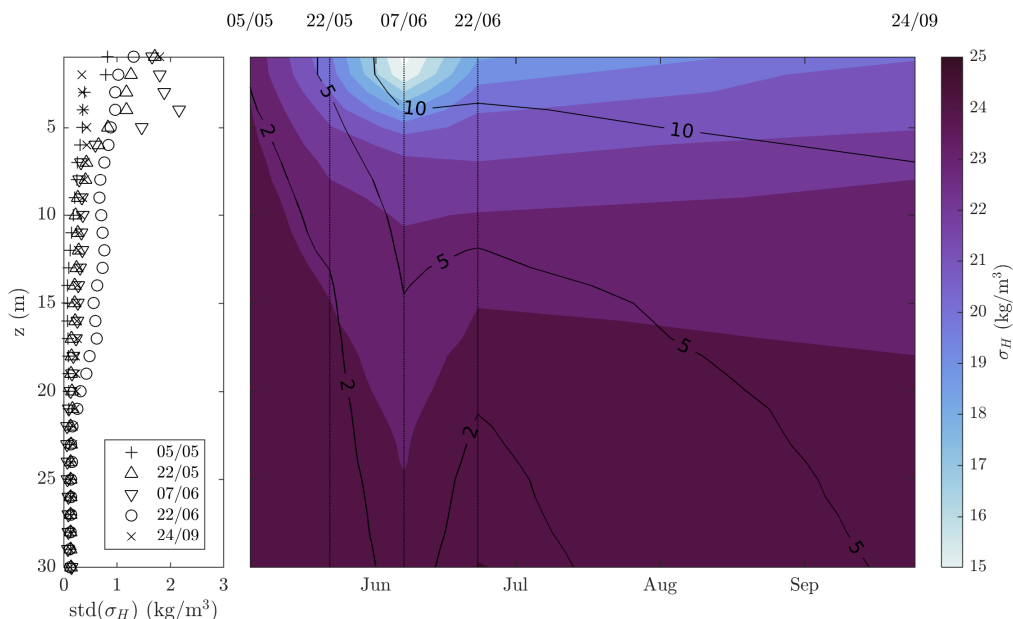
Figure 9: Evolution of the average water column density structure through the season. The color axis shows density, whereas the overlaid solid black lines show temperature. Standard deviation between stations is computed for every campaign and shown on the left. Dashed lines indicate times of sampling campaigns.

Discharge time series of local, regional, and large scale fresh water sources are shown on Figure 10. The yearly mean discharge of the Rapides river is 16.6 m^3 s^{-1} making it the largest contributor (74.4%) to the yearly averaged value for all of BSI's tributaries (22.3 m^3 s^{-1}) presented by Procéan (1999). During peak discharge (April to July) the climatology averages to more than double the yearly value (36.4 m^3 s^{-1}) with the maximum (78.5 m^3 s^{-1}) happening on May 24. As sampling was conducted two weeks apart around the spring freshet, maximum local discharge therefore happened 14±14 days before minimum density was measured in the BSI. The maximum monthly and daily discharges of the St. Lawrence and Moisie Rivers happen respectively 22±14 and 23±14 days prior to the early June measurements (2017/06/07), when minimum salinity was observed in the BSI (S_H = 19.8 PSU, $z < 2$). Daily averaged salinity data from a DFO buoy near Rimouski, upstream of the BSI shows a seasonal minimum of S = 15.7 on May 24.
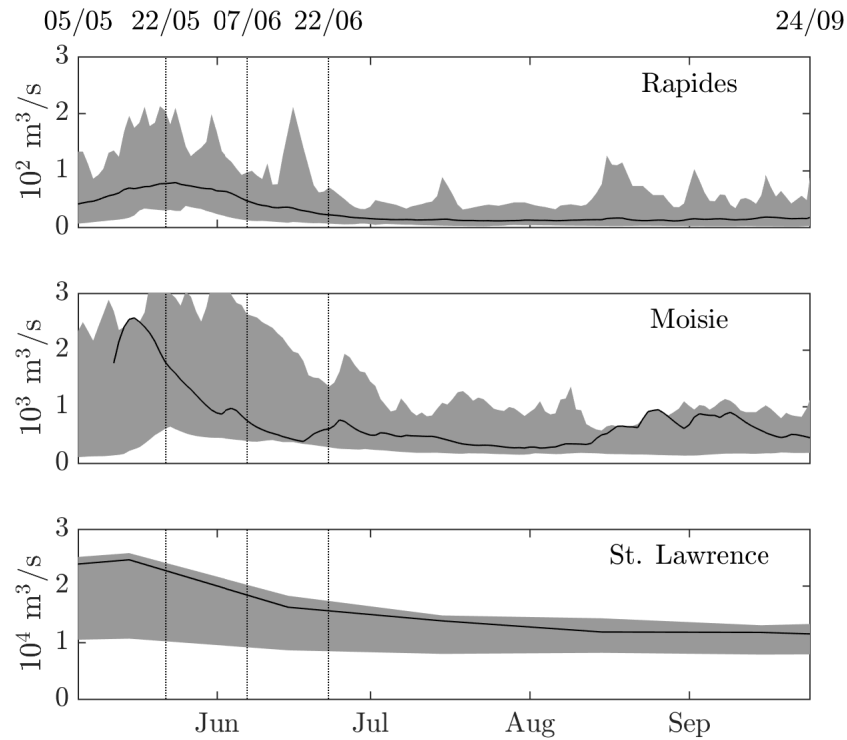
Figure 10: Time series of river discharge for three rivers, Rapide (local), Moisie (regional), and St. Lawrence (large scale). The area between climatological maximums and minimums is shown in grey. For the middle and bottom panels the solid black line shows 2017 values. Since these values are unavailable for rivière des Rapides, the climatology mean is shown. Dashed lines indicate times of sampling campaigns. Top two panels made from CEHQ tide gauge data, and bottom panel shows RIVSUM.

1.4.3.2 Tidal scale

CTD data from the June 2017, September 2017, and May 2018 campaigns is used to reconstruct temperature and salinity fields on T1 at several moments of the tidal phase, as shown on Figure 11. Tidal range during these three measurements was respectively $r = 1.52$ m, $r = 1.42$ m, and $r = 2.34$ m. We define $\Delta T, \Delta S$ positive along x_c, as the temperature and salinity difference between reconstructed profiles averaged over the 5 surface meters at a given time. Its indices define the concerned stations; south ($x_c \sim 1$ km), center ($x_c \sim 2.5$ km), and north ($x_c \sim 4$ km), such that ΔT_{NS} is the difference between temperatures north

and south, ΔT_{NC} is the difference between temperatures north and center, and ΔT_{CS} is the difference between temperatures center and south. Values of ΔT and ΔS are presented in Table 6 for the three reconstructed tide cycles at tide phases matching the panels of Figure 11.

Tidal evolution of the horizontal stratification across T1 seems variable. In June, ΔT_{NS} and ΔS_{NS} were of opposing signs and both switched direction during the tidal cycle. In September and May, ΔT_{NS} and ΔS_{NS} remained in the same direction throughout the tidal cycle, but reached minimums at ebb and low tide respectively. Note however that ΔS_{SN} is of opposite sign during these two measurements.

HT+t	ΔT_{NS} (°C)	ΔS_{NS} (PSU)	ΔT_{CS} (°C)	ΔS_{CS} (PSU)	ΔT_{NC} (°C)	ΔS_{NC} (PSU)
0	-0.44	0.85	-0.24	0.73	-0.20	0.12
3	-0.19	0.81	-0.09	0.40	-0.10	0.41
6	1.31	-0.48	1.07	-0.45	0.24	-0.04
9	0.49	-0.04	0.97	-0.37	-0.47	0.32
0	-0.48	-0.29	-0.47	0.03	-0.01	-0.33
3	-0.37	-0.02	-0.38	0.32	0.00	-0.33
6	-0.37	-0.69	0.05	-0.16	-0.42	-0.52
9	-0.72	-0.61	-0.52	-0.34	-0.21	-0.27
0	-0.81	1.89	-0.47	1.52	-0.34	0.37
3	-0.37	0.61	0.14	0.28	-0.51	0.32
6	-0.22	0.09	0.09	-0.16	-0.32	0.24
9	-0.82	1.38	-0.46	1.09	-0.36	0.29

Table 6: Temperature and salinity difference between the south, center and north sampling stations for the reconstructed tide cycles of June 2017 (top row), September 2017 (middle row), and May 2018 (bottom row). The left column indicates tidal phase in hours after high tide.

The largest ΔT_{SN} and ΔS_{SN} values were measured in June at low tide, and in May at high tide. Both of these maxima have in common that most of the variation happens between the south and center stations. ΔS_{CS} and ΔS_{NC} have been observed in opposition, placing the saltiest water in the center of T1 as in September (HT+3), or to the sides as in June (HT+9) and in May (HT+6). This has also been seen in ΔT_{CS} and ΔT_{NC} notably in June (HT+9) and in May (HT+3) placing the warmer water in the center of T1.
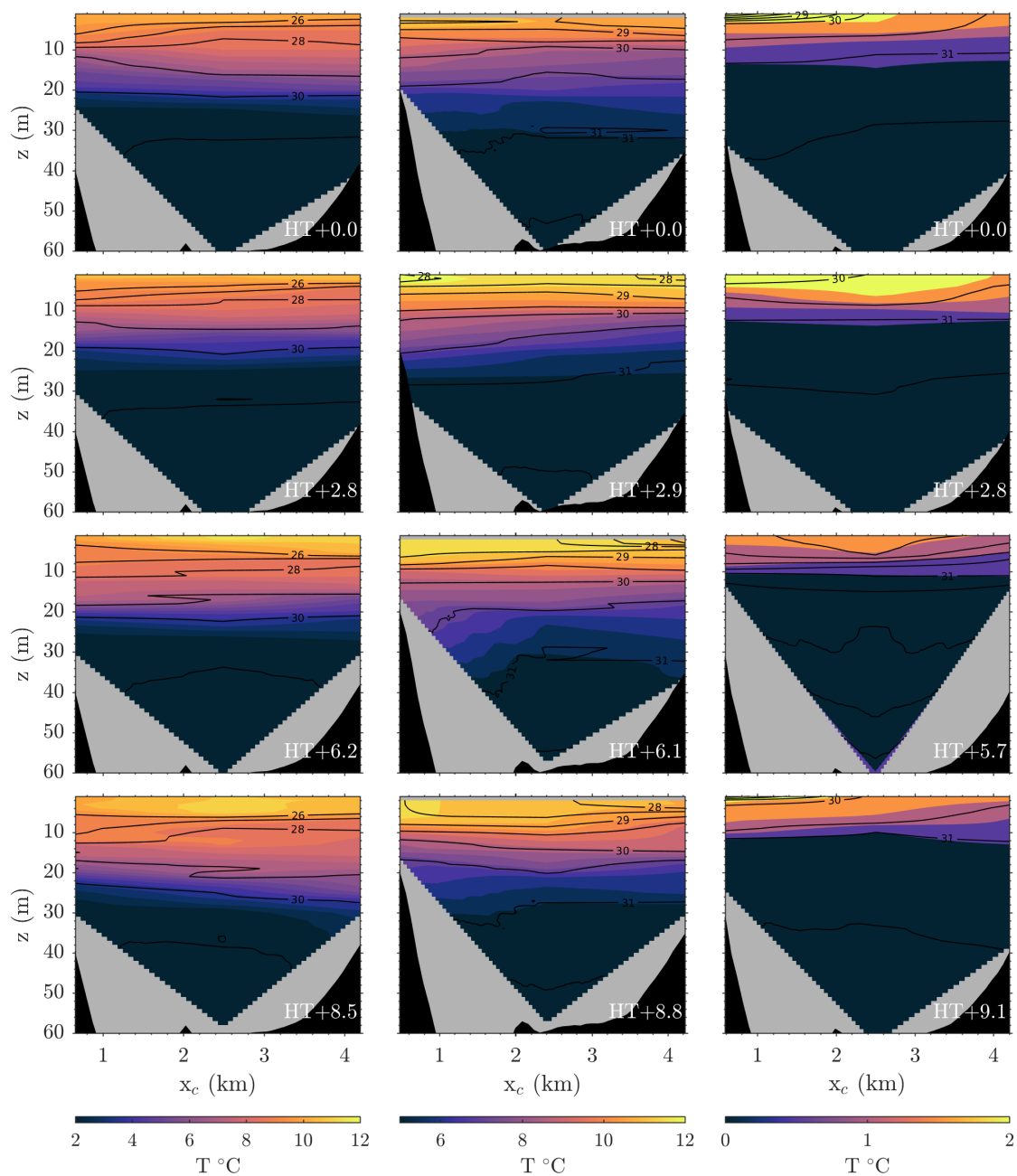
Figure 11: Reconstructed temperature (color) and salinity (solid lines) fields along T1. Columns are June 2017 (left), September 2017 (center), and May 2018 (right) repeated transects. Rows are approximately corresponding tidal phase, as is written in hours after high tide. Note the different color axes for each column.

Tides also bring change in vertical stratification. Maximum N^2 values for the reconstructed south, center and north profiles are shown in Table 7. Median values are $N^2_{max} = 7.0 \times 10^{-3}$ s^{-2}, 3.5×10^{-3} s^{-2}, and 1.7×10^{-3} s^{-2} for the June, September, and May campaigns. Stratification at T1 was therefore overall half as strong in September relative to June, and half as strong in May relative to September. The sharpest stratification ($N^2_{max} = 1.2 \times 10^{-2}$ s^{-2}) was however measured in May at flood tide.

	South		Center		North	
HT+t	N^2_{max} (10^{-3}s^{-2})	z (m)	N^2_{max} (10^{-3}s^{-2})	z (m)	N^2_{max} (10^{-3}s^{-2})	z (m)
0	7.8	9	7.3	4	5.9	3
3	5.4	8	5.7	5	8.2	4
6	3.9	12	4.4	6	8.9	7
9	6.7	13	8.4	6	7.6	6
0	3.7	5	3.3	8	3.6	7
3	3.5	4	2.8	10	3.9	10
6	4.5	9	3.2	6	6.3	4
9	3.3	9	2.5	9	3.9	5
0	9.8	2	1.4	7	0.63	12
3	2.6	1	1.7	9	1.1	13
6	1.6	10	1.9	7	1	5
9	12	1	1.9	9	0.93	12

Table 7: Profile maximum buoyancy frequency south, center, and north of T1, with corresponding depth. The left column shows time after high tide. The top, middle and bottom tiers show June 2017, September 2017, and May 2018 measurements, respectively.

During all three measurements at the north profile, N^2_{max} values tended to be larger at ebb and LSW with respect to flood and HSW. Maximum to minimum N^2_{max} ratios were ~ 1.5, ~ 1.8, and ~ 1.8 for the three campaigns chronologically. For the south profile, the opposite tendency was measured in June and May with maximum to minimum ratios of ~ 2.0, ~ 7.5. The center profile exhibits a tendency similar to the south profile in June and September but similar to the north profile in May.

The temperature and salinity fields shown above may be used with velocity data at the bay entrance to compute throughout the tidal cycle the reduced stratification N^2_r that is,

$$N_r^2 = N^2 - \frac{S^2}{4} \tag{1.14}$$

This quantity is a re-arrangement of the Richardson number criterion for shear instability, $\mathrm{Ri} = N^2/S^2 < 1/4$. Conditions can be considered as being dynamically unstable when $N_r^2 < 0$ and stable otherwise. Figure 12 displays 1.5 h averages of salinity (solid lines) and N_r^2 (color) smoothed by a 4 m vertical moving average, at four tidal phases shown by the inset. The horizontal axis is distance from the southern shore along the transect line. A band of positive N_r^2 spanning the entire transect highlights the dynamically stable pycnocline. Following closely the centre of this stable band through the tidal cycle, the 30.75 PSU isohaline is chosen here as a marker for the pycnocline. Values within 0.05 of this salt content are found at an average depth of 8.7 ± 1.0 m, and characterized by $N_r^2 = 4 \pm 2 \times 10^{-2}$ s^{-2}.

Currents reconstructed from the May 17, 2018 measurements over all of transect T1, time averaged around 4 tidal phases, and vertically binned into three layers are shown on Figure 13. The three depth layers are roughly representative of the region over the pycnocline, the region where the pycnocline resides, and the region under the pycnocline. At high tide, average surface currents ($0 - 5$ m) were pointing downstream ($u_a = 9.5 \pm 7.8$ cm s^{-1}) while deeper currents (15-27 m) pointed towards the inside of the bay ($u_a = -3.8 \pm 7.0$ cm s^{-1}). At ebb tide average currents in the three layers were oriented downstream but were strongest ($u_a = 19.3 \pm 4.0$ cm s^{-1}) near the surface, and weakening with depth to $u_a = 6.5 \pm 5.2$ cm s^{-1} in the pycnocline region, and $u_a = 2.7 \pm 5.6$ cm s^{-1} in deeper waters. Ebb tide is when absolute current speeds were strongest on average ($|\mathbf{u}| = 9.8 \pm 5.8$ cm s^{-1}).
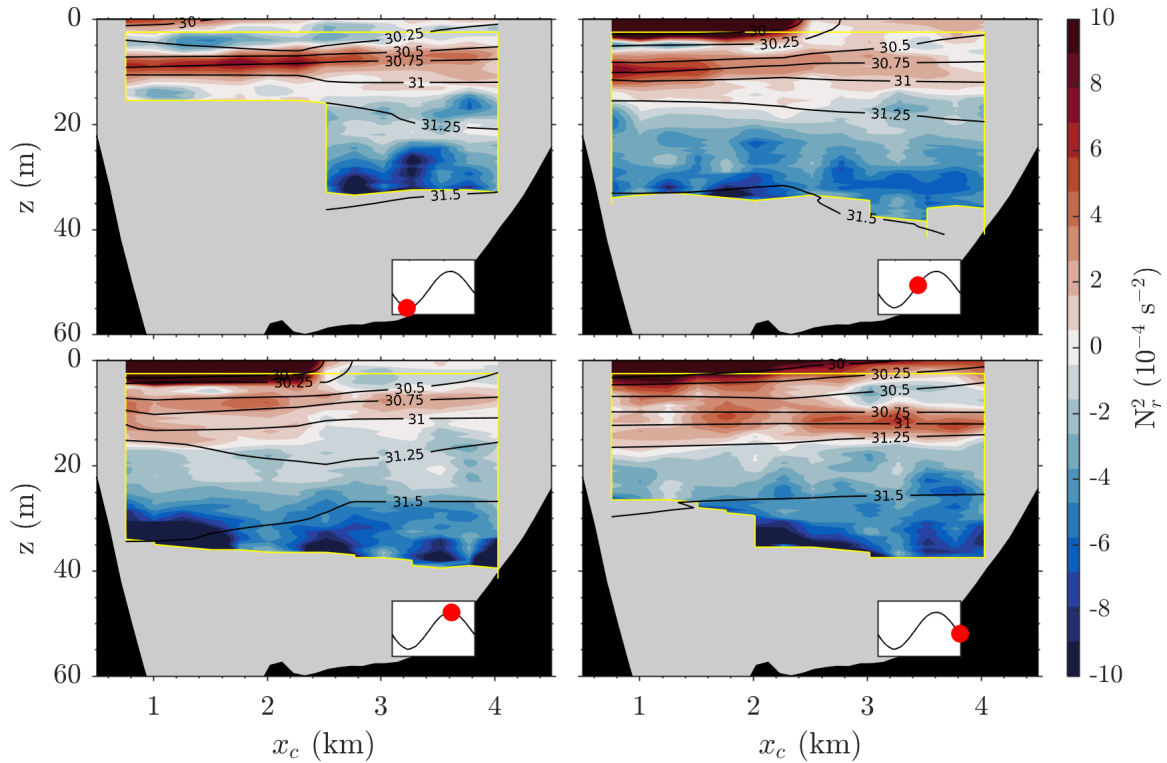
Figure 12: Reconstructed reduced stratification and salinity fields at four tidal phases noted by the inset. Solid lines show salinity while colored contours show reduced stratification. Data inside the yellow line is from measurements and data outside uses extrapolation. N_r^2 is smoothed vertically using a 4 m moving average and a 1.5 hour moving average in time.

The average amplitude of current speeds was lowest at low tide ($|\mathbf{u}| = 7.5 \pm 4.5$ cm s^{-1}). Motion then seems less organised with the exception of a remaining downstream current near Pointe à la Marmite ($x_c < 1.5$ km) in the pycnocline layer ($u_a = 7.0 \pm 6.5$ cm s^{-1}) and above it ($u_a = 4.0 \pm 3.8$ cm s^{-1}). Flood tide reversed currents upstream. The strongest upstream currents ($u_a = -10.1 \pm 3.8$ cm s^{-1}) were in the deep ($15 - 27$ m) southern ($x_c < 1.5$ km) portion of T1. Currents ($u_a = 2.4 \pm 7.0$ cm s^{-1}) were however measured downstream directly above them near the surface (0-5 m). Note that surface currents were measured downstream throughout the tidal cycle near Pointe à la Marmite. In usual alignment with the surface currents, $\bar{u}_a$ begins flowing downstream shortly before ebb tide, and back upstream

shortly before flood tide. Its values are larger during ebb and flood ($\bar{u}_a = 5.6 \pm 0.3$ cm s^{-1}, $\bar{u}_a = -6.5 \pm 1.0$ cm s^{-1}) in comparison to high and low slack water ($\bar{u}_a = 2.1 \pm 2.4$ cm s^{-1}, $\bar{u}_a = -1.2 \pm 2.9$ cm s^{-1}).
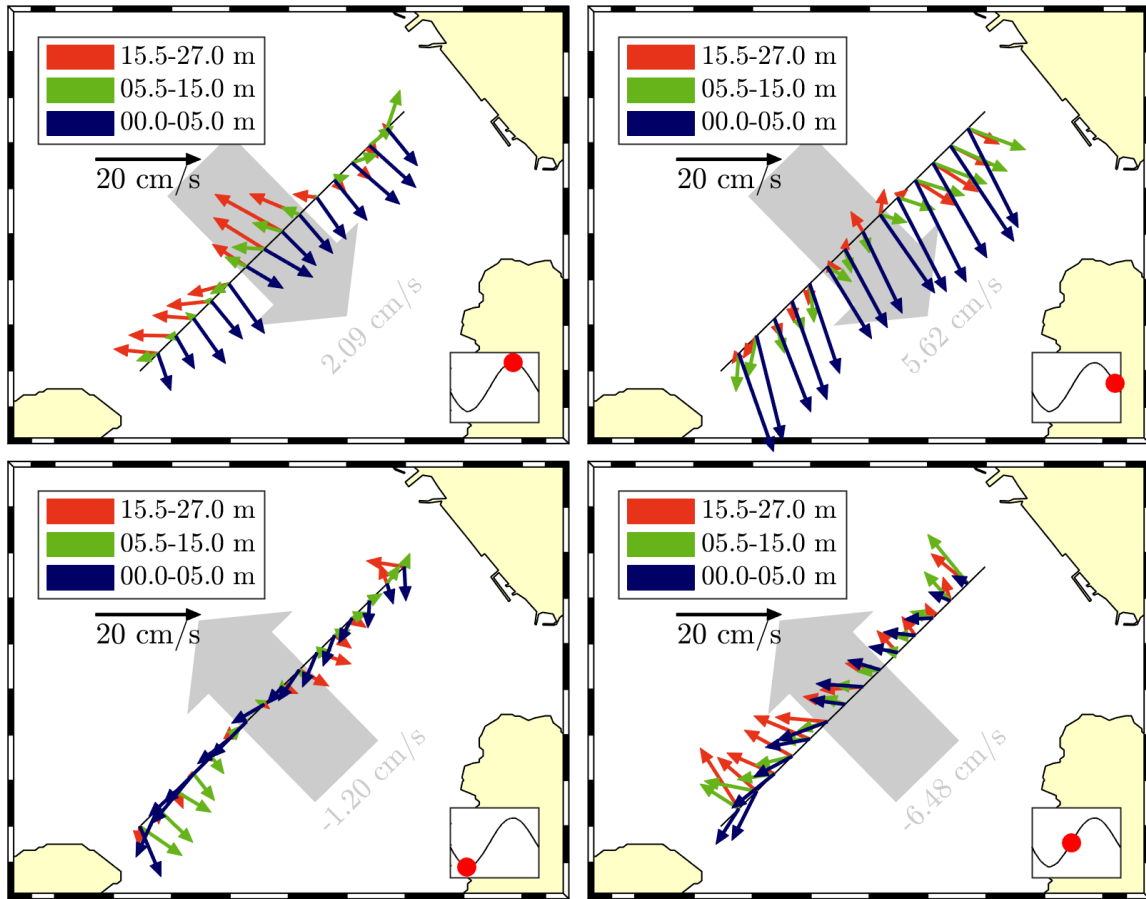
Figure 13: Reconstructed tidal cycle from repeated transects. Vector colors show represented depth layer. Tidal phase is found on the inset. Data is passed through a 3 hour moving time average. Gray arrow shows average cross transect current direction in the unmeasured area, norm is written in matching color.

Reconstructed currents may be averaged to show the net inflow and outflow regions of section T1. The results of this operation are shown in Figure 14 where contours show along shore velocity u_a. Over the pycnocline (0-4 m) water flowed downstream, with stronger currents near the coasts ($\langle u_a \rangle_{12h} = 7.5 \pm 3.0$ cm s^{-1} at $x_c = 0 - 2$ km, and $\langle u_a \rangle_{12h} = 7.7 \pm 2.0$ cm s^{-1} $x_c = 3 - 5$ km), and slower currents near the center ($\langle u_a \rangle_{12h} = 5.2 \pm 1.3$ cm s^{-1}

at $x_c = 2 - 3$ km). Note the standard deviation here is on the spatial average but not the time average. Between $z = 5$ and 13 m, currents were more spatially variable but dominantly out flowing near Pointe à la Marmite ($\langle u_a \rangle_{12h} = 2.6 \pm 3.8$ cm s^{-1} at $x_c = 0 - 2$ km) and in flowing everywhere else ($\langle u_a \rangle_{12h} = -0.6 \pm 2.1$ cm s^{-1}). The bottom layer, in phase with $\bar{u}_a$ when averaged over 12 hours ($\langle \bar{u}_a \rangle_{12h} = -0.2$ cm s^{-1}), was measured mostly inflowing ($\langle u_a \rangle_{12h} = -2.1 \pm 4.0$ cm s^{-1}) with the exception of a band of out flowing water spanning from the pycnocline until the sea floor ($12 - 40$ m), between $x_c = 2.7$ and $x_c = 4$ km.
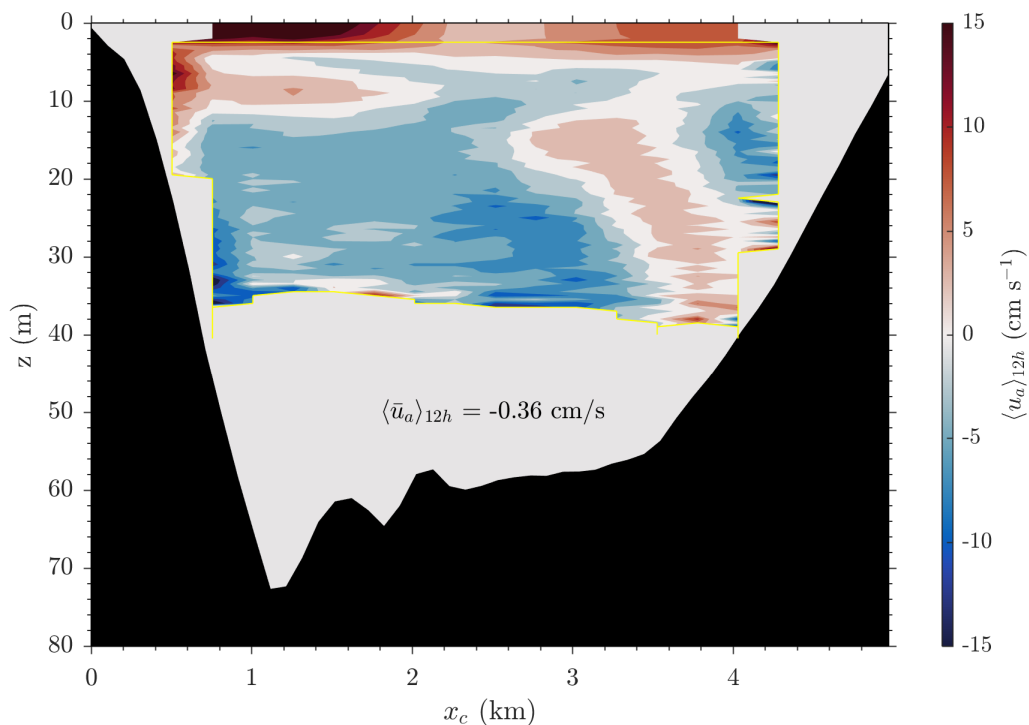
Figure 14: Along shore velocity averaged over 12.5 hours. Speed values inside the yellow contours are from measurements.

Friedrichs and Aubrey (1996) showed that an estimate of the maximum contribution of the tidal currents to cross shore velocity on tidal flats can be drawn from geometrical considerations, conservation of mass, and sea level data. As reformulated by Hir et al. (2000) for a straight coast and linearly sloping topography, this estimate is given by

$$u_{\max}(x_f) = \frac{\pi r}{\zeta P} \sqrt{1 - \left[\frac{2\zeta}{r} x_f\right]^2} \quad , \quad x_f > 0$$

$$u_{\max}(x_f) = \frac{\pi r}{\zeta P} \quad\quad\quad , \quad x_f < 0 \tag{1.15}$$

where r is the tidal range, P the tidal period, ζ the bathymetry slope assumed small, and x_f the distance of the tidal front to its mid tide position. In this framework, cross shore currents are being modelled as movement of the tidal front implying that fastest velocities happen at mid tide ($x_f = 0$). The top statement of equation 1.15 reflects how the tidal front decelerates as it moves from the mid tide to the high tide line. The bottom statement represents the assumption that current in waters deeper than the tidal front follow it at the same speed and therefore peak when $x_f = 0$. Figure 15 shows the computed values on the BSI tidal flat during spring tide, with r set to 3.5 m. The origin of x_f was placed at the average sea level $z = 1.6$ m. The value of x_f was computed in the direction of ζ for every point.
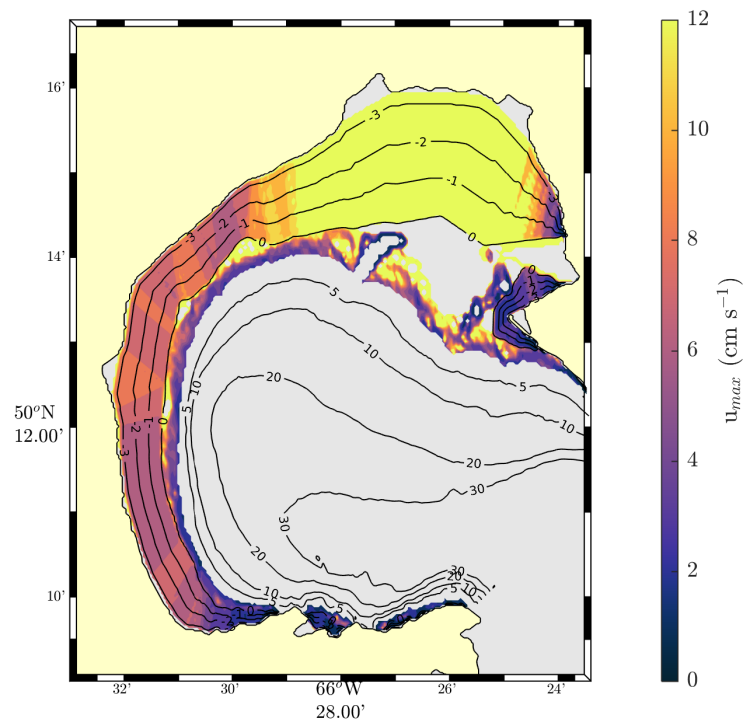
Figure 15: Maximum cross shore velocity estimate during spring tide (amplitude = 1.755 m) shown by the color axis. Overlaid black coutours are bathymetry.

The computed cross shore velocities average to $u_{\mathrm{max}} = 11.6 \pm 7.4$ cm s^{-1}. Larger velocities (~20 cm s^{-1}) are found in the north portion of the bay where the interpolated flat is widest, however bathymetric data is most sparse in this area. On average $u_{\mathrm{max}} = 7.3 \pm 3.7$ cm s^{-1} for the western flat (longitude < -66.5°). For average and neap tide ranges of (1.9 and 0.5 m), the average speeds estimated on the western flat are $u_{\mathrm{max}} = 3.5 \pm 3.0$ cm s^{-1}, and $u_{\mathrm{max}} = 0.8 \pm 0.2$ cm s^{-1}.

1.4.4 Spatial variability

The spatial distribution of drifter tracks is shown in the top left panel of Figure 16. This representation highlights how drifters launched anywhere inside the bay rarely venture to the northern portion near the river mouths. Most (4/7) drifters placed at the mouth of River Rapides headed south-west across the bay. While they were crossing, average winds were northerly (3.3 ± 1.6 m s^{-1}, towards 188°). Another deployment from the same site was conducted under northwesterly wind of comparable strength (4.3 ± 0.9 m s^{-1}, towards 138°) and both drifters followed the eastern shore instead. On average, drifters placed near the river mouths that did not beach were flushed (latitude $< 50.22°$) within 6.0 ± 0.6 hours of deployment. Many drifter trajectories (22 out of 46) ended their course on the west and south-west shores of the bay as can be seen from the high density of crosses in Figure 16. These results may be explained by drifters following the path of river discharge along the western shore. Note as well that many drifters beached on shores opposing two of the identified prevailing wind conditions in summer (NNW and ESE).

To highlight bay scale features, the drifter speeds were spatially averaged as in Richardson (1983) and Martins et al. (2002). Vectors on Figure 16 show the result of this analysis using 1.5 km square boxes, with the red ellipses tilt and axes showing principal directions of variation and their associated magnitude. Drift data outside the boxes was accounted for in the nearest box.

The top right panel shows all drifter data averaged. Distinguishable features include a current originating in the northern part of the bay near Rapides river and running along the western and southern shores until exiting the bay through the southern portion of its mouth. There is another current entering the bay through the northern part of its mouth and running diagonally towards the north west. Ellipses are aligned with the shores in the south and west portions of the bay showing currents there are mostly alongshore.
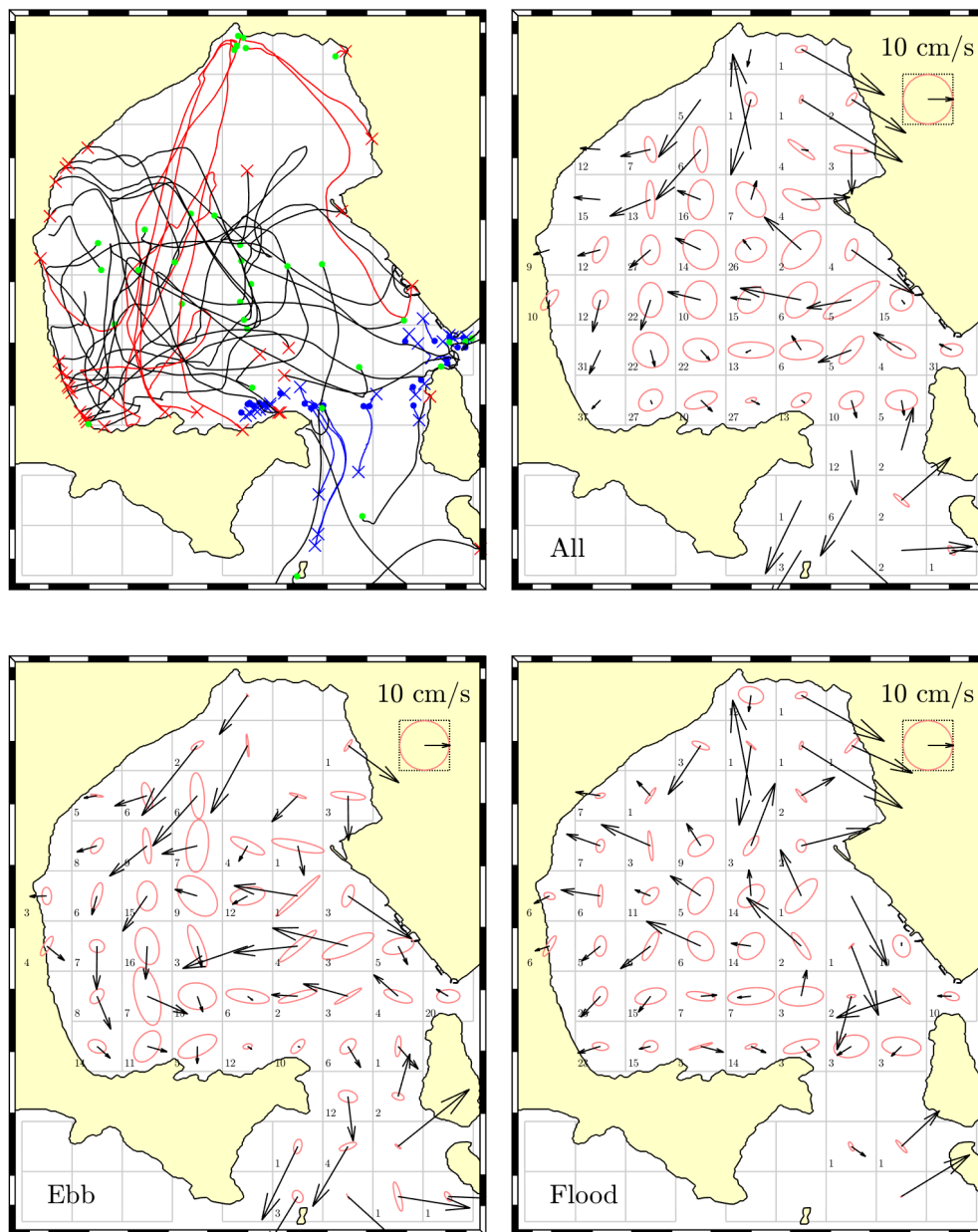
Figure 16: Drifter tracks and their box averaged speeds. Ellipses follow the same scale as arrows and show standard deviation in the two principal axes of variation. Dots and crosses show deployment and last ping respectively. Blue tracks are the DFO measurements from 2003, red tracks are purposely put at the mouth of rivers, and black tracks are ship borne deployments. Numbers are cumulative hours of drift per box. Left and right bottom panels are box averages for ebb and flood data.

The bottom panels of Figure 16 are averages over the same grid using only data from ebb tide (left) and flood tide (right). The most striking difference between these two panels is seen near the western shore, where along shore currents seem prevalent during ebb tide while cross shore currents dominate the flood tide phase. During flood, average circulation seemed directed towards the shallow tidal flats while at ebb, average circulation followed an anticyclonic pattern. Outflow near Pointe à la Marmite appears both in average flood and ebb drifter data.

The eastward speed is roughly cross shore west of 66°30′W. Eastward drifter velocities there average to -8.8 ± 6.7 cm s^{-1} during flood. The cross shore speed estimates of the previous section for this tidal flat therefore account for 83%, 40%, and 9% of the average cross shore velocity during spring, average, and neap tide respectively. Almost half of the observed shoreward velocity in typical conditions can thus be explained by change in sea level and the shape of the tidal flats.

A probability distribution for surface current speeds is drawn from the drifter data and shown in the top panel of Figure 17. Data south of latitude 50.05°N is considered outside the bay and omitted from this figure and the following statistics. Average drifter speed is 17.4 cm s^{-1}. Speeds have been measured up to 86.6 cm s^{-1} but are only greater than 50 cm s^{-1} in 1.63% of cases. Median and maximum drift duration were 12.7 ± 7.5 h, and 71.5 h. Drifts with durations longer than 1, 2, and 3 tidal cycles make up 54%, 10%, and 4% of drifts respectively. The distribution of ADCP velocities measured during one tidal cycle along T1 and inside the surface 9 m, and below are shown in the middle and bottom panels. Average speed for the surface 9 m is lower (9.6 cm s^{-1}) with respect to drifter data, but greater than deeper velocities (8.6 cm s^{-1}).
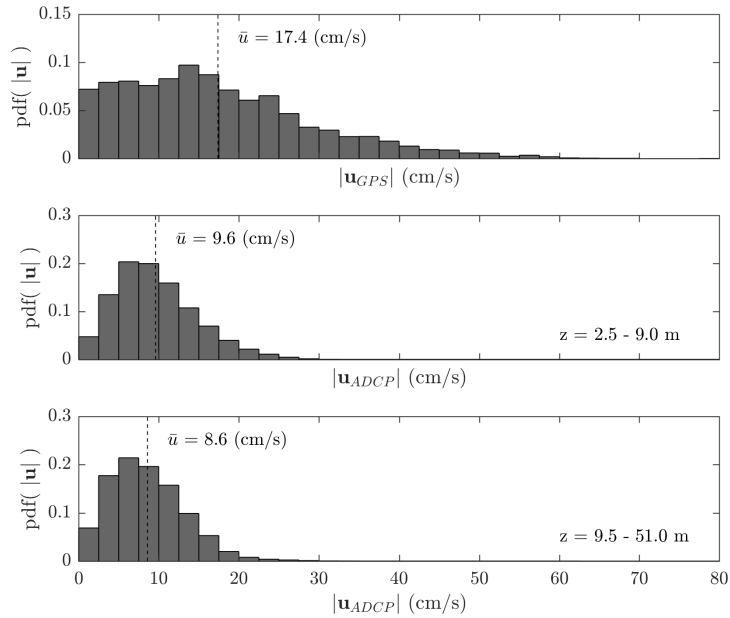
Figure 17: Probability density distribution for speed amplitudes of all drifter data recorded north of 50.05° (top), T1 ADCP data in first 9 m (middle), and the rest of the water column (bottom). Average values are shown by the dashed line.

A global view of the relationship between drifter heading θ_d and wind direction θ_w is provided through projection onto a toroidal surface, shown in Figure 18. High wind speed data appears gathers near the 1:1 ratio line especially in directions where data density is high. The coefficient $\rho = |\rho|e^{i\phi}$ proposed by Kundu (1976) is a complex number whose amplitude $|\rho|$ and phase ϕ respectively describe the strength of correlation and phase difference of two complex time series (e.g. horizontal velocities). Its amplitude ranges from 0 to 1 with the latter expressing perfect correlation. Its phase describes the typical angular difference between the time series, and is only meaningful if correlation is reasonably high. This measure of correlation was computed individually for all drifts and when averaged, gives $\rho = (0.45 \pm 0.26)\exp(-22 \pm 30i)$. This number however increases to $\rho = (0.59 \pm 0.21)\exp(-24 \pm 39i)$ for data when wind was faster than the annual average (> 4 m s^{-1}), suggesting the wind was 24±39 degrees east of drifter velocity. Though the

phase difference is small, the large spread around it along with relatively low ρ values show surface currents to be in coarse alignment with the wind, rather than to be typically controlled by it, even during stronger than average wind conditions.
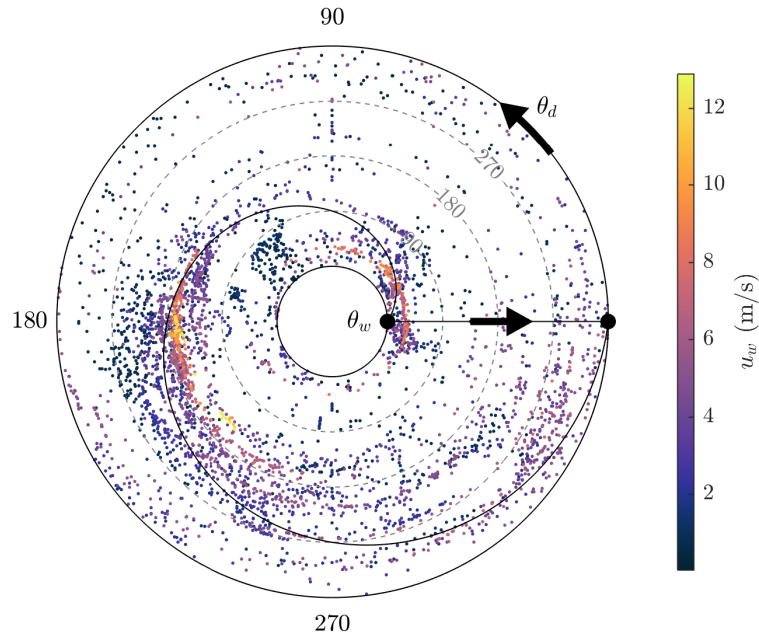
Figure 18: Toroidal projection of drifter heading θ_d plotted against wind heading θ_w (0°=E, 90°=N) interpolated in time and space. Black dots indicate the origins of axes θ_d and θ_w, respectively running counter clockwise, and from the inside out. The color axis highlights corresponding wind speed and the solid black line marks the 1:1 ratio.

For weather related reasons, the underway ADCP measurements along T2, (Figure 2) were interrupted and resumed two days later at similar tidal phase (flood) and luckily, under similar wind conditions. Currents vertically averaged for the layer above the pycnocline, under the pycnocline, and depth averaged vertical velocities, interpolated onto a regular 252 m square grid, are shown on Figure 19.
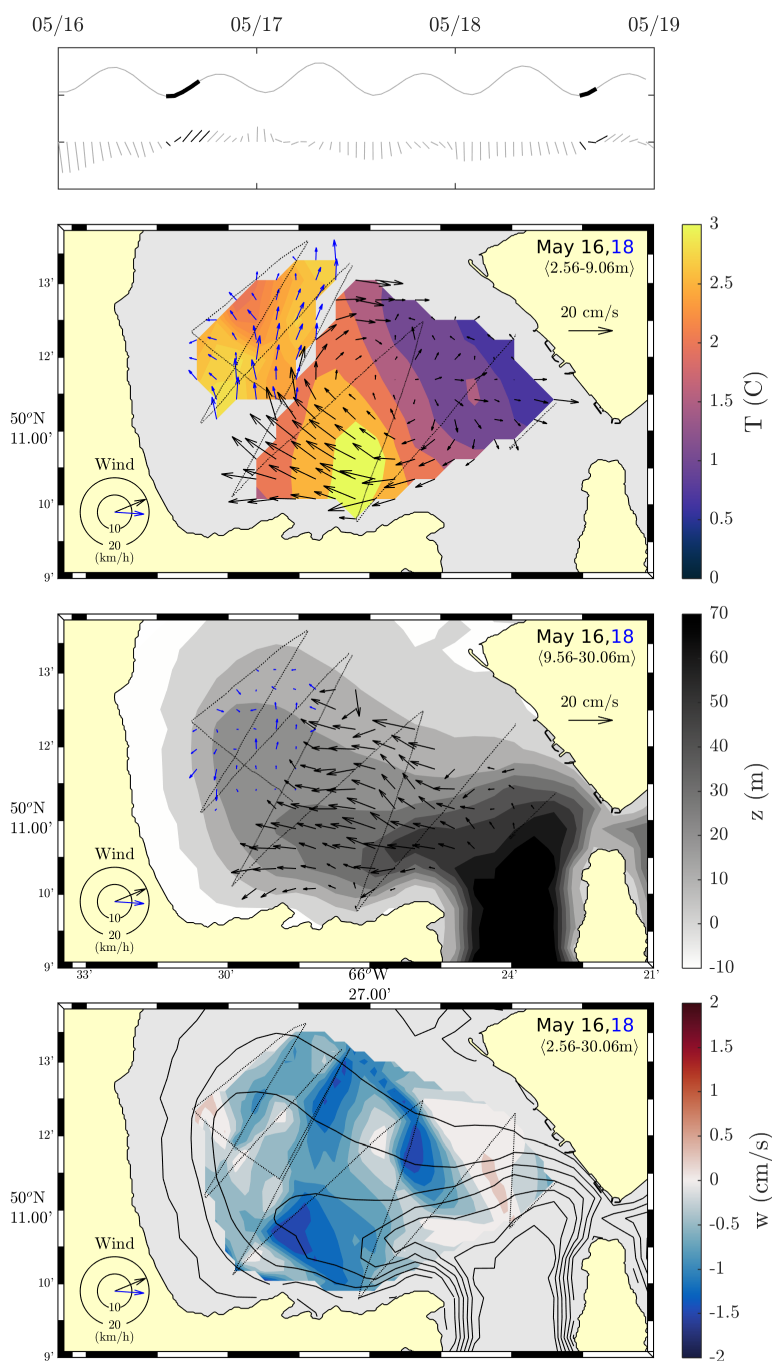
Figure 19: Interpolated synoptic image of ADCP measurements inside the bay. On the top panel, time of sampling is highlighted in black over the sea surface elevation curve, and wind feather plot. Mean wind vectors during these measurements are shown on the bottom left. The second, third and last panels from the top show mean surface layer speeds, bottom layer speeds, and depth averaged vertical velocity (positive downwards) respectively. Vector colors note the day of measurement, ship track is shown by the dashed line and the color axis shows temperature (second panel), depth (third panel), and *w* (bottom panel).

A bay scale anticyclonic current was measured on May 16 (second panel from top), the center of which was located near a horizontal temperature front. While no assessment may be made of the current's persistence, temperature and velocity fields from May 18 follow the prior data with striking continuity. Dynamics in the bottom layer were found to be different, flowing inward over the measured area in general alignment with bathymetric lines. Depth averaged vertical velocity is measured mostly (75%) upward, notably in the south of the bay where bathymetry seems to steer the bottom layer current. The vector field is far less continuous for these depths in direction and amplitude, when compared to the top layer. The wind rose on the lower left shows direction and magnitude averaged over the study area during the time of measurements. While May 16 was host to stronger speeds at 5.7 m s^{-1}, relative to 4.8 m s^{-1} two days later, both winds were westerly.

1.5   Discussion

1.5.1   Influence of Earth's rotation

In stratified basins, the influence of the Earth's rotation on hydrodynamics can be evaluated by scaling the internal Rossby deformation radius. This is defined by Pedlosky (1987) as

$$L_D = \frac{(g'D)^{1/2}}{f_0} = \left[\frac{gD}{\bar{\rho}}\frac{\partial\rho}{\partial z}\right]^{1/2}\frac{D^{1/2}}{f_0} \qquad (1.16)$$

where the reduced gravity g' corresponds to the bracketed term, $g = 9.8$ m s^{-2} is the gravitational acceleration, $f_0 \sim 10^{-4}$ s^{-1} is the Coriolis parameter, D is depth, and ρ is density. For a two layer system this becomes,

$$L_D = \left[g\frac{\rho_2 - \rho_1}{\bar{\rho}}\right]^{1/2}\frac{D_1^{1/2}}{f_0} \qquad (1.17)$$

with ρ_2 the bottom layer density, ρ_1 the surface layer density, and D_1 the surface layer thick-

ness. Its stratification (see Figures 7, 11, and 12) and currents (see Figures 13, and 14) suggest the inside of the BSI may be approximated as a two-layer system. The reduced stratification analysis from section 1.4.3.2 and visual inspection of average density profiles for CTD casts inside the bay in early May (weakest stratification) and early June (strongest stratification) suggest $D_1 \sim 10$ m as an upper bound to surface layer scale. Averaging densities for these profiles yields $\rho_1 = 1023.95$ kg m^{-3}, $\rho_2 = 1024.77$ kg m^{-3}, and $\bar{\rho} = 1024.45$ kg m^{-3} in low stratification, and $\rho_1 = 1019.23$ kg m^{-3}, $\rho_2 = 1024.02$ kg m^{-3}, and $\bar{\rho} = 1022.09$ kg m^{-3} in high stratification. The internal Rossby deformation radius was therefore $L_D = 2.8$ km in May, and $L_D = 6.8$ km in June.

A 10 km horizontal scale is appropriate for the surface of the bay, however from north to south, the portion of the bay deeper than 10 m is closer to 6 km. Comparing L_D to the surface scale shows influence of Coriolis acceleration on surface currents be neglected neither during strongly stratified conditions measured in June nor the more common weakly stratified condtions measured in May. Near the pycnocline depth, $L/L_D \sim 2.1$ in May and $L/L_D \sim 0.9$ in June. Phenomena related to earth's rotation may still be expected under weak stratification but are unlikely under strong stratification.

1.5.2   Fresh water input

Even though a discharge time series for the rivers flowing into the BSI is unavailable, the climatology values for rivière des Rapides may be used to evaluate their capacity to produce the low salinity values observed in early June. Supposing i) that the fresh water is completely mixed before exiting the bay, ii) that it is mixed only in the top 20 m as suggested by Figure 9, and iii) that it is accumulated much faster than it is evacuated, iv) that the net freshwater brought through T1 over a tidal cycle can be neglected, the fresh water volume necessary can be approximated to a dilution such that,

$$V_f = V_{20} \left(\frac{S_m}{S_j} - 1 \right) \tag{1.18}$$

where S_m and S_j are the average salinities in the surface 20 meters for the early May and early June campaigns, V_f is the fresh water volume, and V_{20} is the volume contained in the 20 surface meters. Using $V_{20} = 0.8$ km^3, $S_m = 30.4$, and $S_j = 27.1$ yields $V_f = 9.68 \times 10^7$ m^3. If applied to the period between May 6 and June 6 this would require a mean discharge of 37.4 m^{3}s^{-1}, which rivière des Rapides on its own can supply as the climatology average for this period is 64.2 m^{3}s^{-1}. A more realistic method is to gradually dilute V_{20} from S_m to S_j by time stepping,

$$S(t + \Delta t) = S(t)\frac{V_{20}}{V_{20} + V_f(t)} \qquad (1.19)$$

where V_f is computed by multiplying Δt with the river discharge from the climatology at time t. The volume prior to dilution is reset to V_{20} at every step, implying a portion of the mixed fresh water escapes the bay. This is therefore expected to require more fresh water before S_j is reached. Once $S(t)$ has been brought to S_j, the cumulative V_f is 9.72×10^7 m^3. This happens on May 23, 14 days prior to the measured minimum density values, again suggesting the rivers are capable of supplying enough fresh water to produce the measured change in stratification in the required time frame.

1.5.3 Flushing time

The bulk time necessary to renew all the BSI's water, often called flushing time or τ, can be computed in a variety of ways. The tidal prism method assumes the volume of water brought in during flood Δ is completely mixed with the basin's water and flushed during ebb. Under this assumption the flushing time is given by

$$\tau = \frac{V + \Delta}{\Delta}P \qquad (1.20)$$

where V is the basin's volume, and P is the tidal period (Dyer, 1973). Inwards of T1, the BSI contains 1.1 km^3 of water. Multiplying surface area with neap, spring, and average tidal ranges gives $\Delta \sim 0.05$ km^3, $\Delta \sim 0.4$ km^3, and $\Delta \sim 0.2$ km^3. River contribution can be

neglected as it is of the order of 10^{-4} km^3. These values result for neap, spring, and average tidal range in τ = 11.9, 1.9, and 3.4 days. Drawbacks of this method are that it fails to account for water re-entering on the next flood, and that complete mixing of Δ is rarely a valid approximation especially in stratified conditions (Dyer, 1973). For both reasons, this method is known to underestimate flushing time.

Another way to compute τ is the salt budget method. It divides V by the inward transport computed using Knudsen's relations for a two-layer system. Flushing time then becomes

$$\tau = \frac{V(S_2 - S_1)}{S_2 R} \tag{1.21}$$

where S_2 and S_1 are the bottom and surface averaged salinities and R is the mean river transport (Dyer, 1973). Averaging salinity where tide averaged speeds were out flowing and in flowing in May 2018 (see Figure 14), respectively provides S_1 = 30.8 and S_2 = 31.3. Using then R = 22.3 m^{3}s^{-1} yields τ = 9.7 days.

When tide averaged velocities are known at the basin's ocean boundary, inward or outward transport can alternatively be used to determine turnover time, which is the same as flushing time assuming a steady state (Talley et al., 2011). Flushing time is therefore

$$\tau = \frac{V}{(\alpha - n\gamma)\langle \bar{u}_a \rangle_{12h} + \sum_{i=1}^{n} \gamma u_i} \tag{1.22}$$

where u is the inward or outward velocity perpendicular to the ocean boundary from the ADCP measurements, γ, α, and n are defined as in section 1.3.3. Note that since $\bar{u}_a$ was inward when averaged over 12 h, it is only used in the calculation of τ using inward transport. The associated term in equation 1.22 is set to zero for computation of τ from outward transport. Using the data from May 2018 (Figure 14), gives τ = 4.2 and τ = 5.1 days using inward and outward transports respectively.

Though there is some scatter, the methods used scale τ to several (1.9 − 11.9) days. Shorter flushing times would be hard to argue for when more than 10% of surface drifters

remained afloat inside the bay longer than 1 day, especially considering that many of them shoaled and did not escape the bay before transmissions ended from mechanical problems or end of battery life. For comparison, $\tau = 23$, and $\tau \sim 10$ days were evaluated by Holloway (1996) and Llebot et al. (2014) for enclosed bays of similar dimensions.

It is worth mentioning that methods which produce a position dependent τ, using outputs from circulation models are more frequently found in the recent literature than bulk values (Du and Shen, 2016; Safak et al., 2015; Zhu et al., 2015).

1.5.4   Current forcing

Coarse alignment of with wind direction with drifter heading (θ_w 24 ± 39° east of θ_d, winds > 4 m s^{-1}) shows that wind influences surface current direction but does not control it. The internal Rossby radius has been computed to $L_D = 2.8$ km and $L_D = 6.8$ km for low and high stratification respectively. This suggests the influence of the earth's rotation can not be neglected, though no clear sign of its influence has been noted in the collected data. Topography seems to play a key role in guiding currents. This can be seen in Figure 16, where most of the variability is alongshore for both western and southern BSI surface currents, as well as in Figure 19 where currents follow bathymetry in the bottom layer, and coast line in the top layer. Along shore currents at the BSI mouth evolve in phase with the tide, showing its influence can be dominant locally. The large variety of surface drifter tracks obtained however suggest that elsewhere, currents are the result of the tide's complex interaction with other forcing sources.
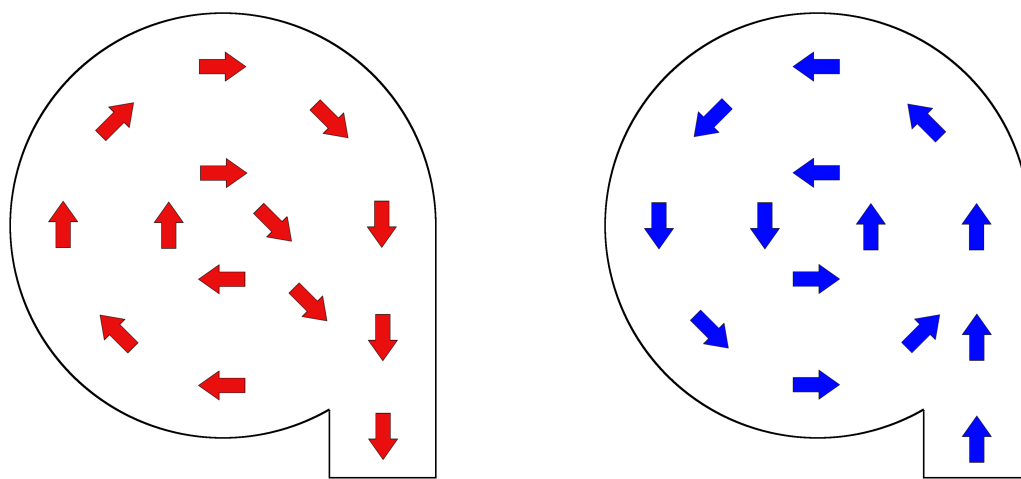
(a) Roche model ebb currents.

(b) Roche model flood currents.
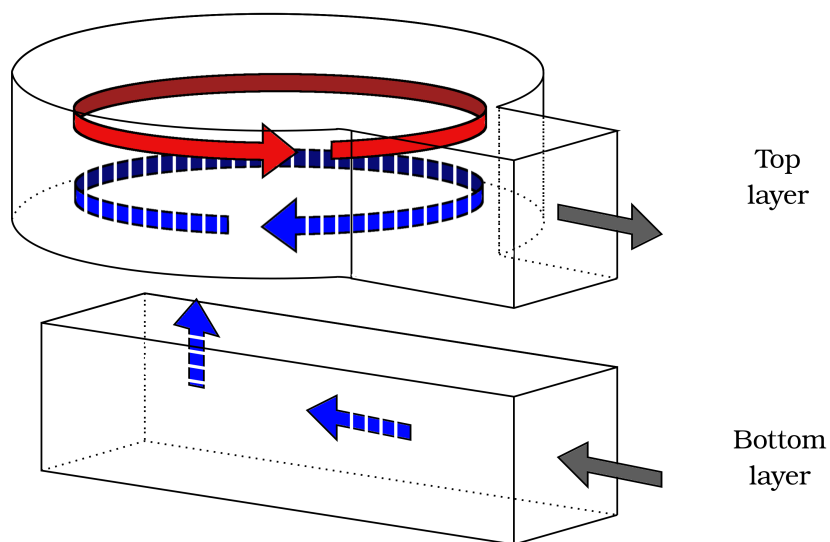
(c) Current observations of summers 2017 and 2018.

Figure 20: The Roche (2000) conceptual model for a) ebb and b) flood currents, and c) our proposed schematic synthesis of the observed BSI circulation. North is towards the top of the page in a) and b). In c) the bottom layer follows the east-west axis. Red, blue and gray arrows stand for ebb, flood and tidally averaged currents. Full arrows designate averages from one or more tidal cycles. Dashed arrows represent an assessment made from a single measurement.

1.5.5   Towards a conceptual circulation model

ADCP measurements from May 16, 2018 (see Figure 19) raise several questions with respect to the conceptual model (Figure 20a, b) for circulation in the BSI, proposed by Roche (2000). At depth, observed flow during flood tide is not circular as was suggested, but rectilinear towards the inside of the bay. While their assessment that flow should follow bathymetric lines still holds at depth, their approximation of the bay as a circular tank is unrealistic as the dimensions of the flow area become increasingly asymmetrical. As this assumption is fundamental to their reasoning and is not supported by observations, their conclusions may be limited to near surface currents. Measurements near the surface are however also problematic since a bay scale anti-cyclonic current was measured on flood tide. Although flow following the cylindrical shape of the container seems an adequate approximation here, the direction of flow is opposite to what their model predicts. Since observations suggest that their model may be limited to the surface currents, and that it is at least wrong on occasion, further thought needs to be given into a conceptual model of hydrodynamic circulation in the BSI.

While data presented here may not be sufficient to support a complete model for the dominant circulation patterns, it allows formulation of dynamical conditions that it should include. These conditions are summarized visually in Figure 20c. Stratification data obtained throughout the season (see Figure 7) shows the BSI should be thought of as a two layer system. The top layer should roughly represent the first 9 m as found by analysis of N throughout a tidal cycle at the bay entrance (Figure 12). Bathymetric data shows that the shapes of these layers are different. For the top layer, a symmetrical shape, such as the cylinder proposed by Roche (2000) is appropriate, but the bottom layer is more elongated, mostly following the southern shore. Currents seemed guided by the shores containing them as seen from the surface circular patterns in Figures 16 and 19, as well as the bottom layer linear pattern shown in Figure 19. Currents were also measured upwards during flood at the western end of the bottom layer, where the bay gets shallower (Figure 19). Currents at the

bay's mouth were not measured heading north as proposed by the Roche (2000) model, but rather entering and exiting along the northwest-southeast axis (see Figures 13, 16, 19). The bay entrance should therefore not be modelled as off-axis as in Roche (2000), but oriented accordingly. Circulation at the bay mouth should be considered estuarian in nature as shown in Figure 14, though further measurements would be required to assess the variability of this condition.

1.6 Conclusion

The objective of this study was to assess spatial and temporal variability of hydrodynamic conditions in the BSI. This has been achieved through collection of two underway ADCP transects, 185 CTD profiles, and 560 hours of surface drift as well as complementary analysis of 46 years of tide gauge data and 1 year of wind model output.

Correlated at $R = 0.99$ throughout the summer season, salinity is shown to be a good predictor of density. Spring runoff causes a disturbance of stratification felt mostly in the top 20 m. This disturbance can change density up to 25% of its summer mean value. Effects of this disturbance lasted less than one month and were centred in early June±two weeks, in 2017. Minimum salinity values happened 14±14, 22±14, and 23±14 days after maximum discharge values for the Rapides river climatology, the St. Lawrence river in 2017, and the Moisie river. The volume of fresh water required to produce this salinity minimum has been shown to be within what the BSI's tributaries can provide in the required time frame. CTD and ADCP data have allowed estimation of flushing time for the BSI using three different methods. The three methods suggest $\tau = 2 - 12$ days. Reduced stratification studied during one tidal cycle shows the pycnocline at the bay mouth at an average depth of $z = 9 \pm 1$ m.

When averaged over a tidal cycle at the BSI mouth, circulation was estuarian. Fresh water flows outward in the top 5 m and mainly flows inward at depths > 15 m. Near the river mouths in the northern part of the BSI, there is a shallow area where currents rarely advect

our surface drifters. Drifters placed in this area are quickly evacuated suggesting seaward circulation. 22/46 drifts end by shoaling on the western and southern shores, showing surface currents are often oriented towards them. This may be due to the dominant wind directions identified by analysis of wind model outputs, especially considering drifter heading was $24 \pm 39°$ west of wind direction on average for drifts when wind speed was > 4 m s^{-1}. Surface currents showed an average speed of 17.4 cm s^{-1} and maximum speeds of 86.6 cm s^{-1}. A current following the western and southern shores to exit near Pointe à la Marmite has been measured in both drifter and ADCP data.

Criticism of the conceptual circulation model proposed by Roche (2000) has been made in light of our measurements. Since this model is qualitatively in opposition to some of our measurements, a new conceptual model of the BSI circulation should be proposed and key elements that this model should include are that this model should:

- have two layers, with the first occupying the top 9 m.
- feature a circular geometry in the top layer.
- feature a rectilinear geometry in the bottom layer.
- feature an estuarian circulation at the bay's mouth.
- explain average cyclonic circulation during ebb.
- explain occasional anti-cyclonic circulation during flood.

Greater insights into the hydrodynamics of the BSI could otherwise be found through the use of a full 3D numerical model, which could be calibrated using the data presented here. Combinations of neap, spring, and average tidal forcing with typical NNW, ESE, and SW winds could be run to identify circulation patterns associated with summer conditions. These experiments could further be run using the stratification measured in early May and early June to detail the impact of weak *vs* strong stratification on these patterns. Neap and spring tide conditions could be compared without wind forcing to isolate the role of tides on circulation. Numerical modelling would also allow assessment of a space dependent residence time and validation of the bulk values presented here.

1.7 Acknowledgments

CONCLUSION GÉNÉRALE

Ce projet se présente à son dénouement dans une forme assez différente de celle proposée au moment du devis de recherche. L'ampleur en était alors beaucoup plus grande et seule une fraction de ce que nous voulions réaliser se trouve dans les pages qui précèdent. Au départ, il était prévu de partir de rien et de livrer un modèle numérique de circulation fonctionnel pour la baie de Sept-Îles après deux ans de travail. La collecte et l'analyse des données devaient être complétées à la fin de la première année du projet et les données devaient servir à valider le modèle développé durant la deuxième année. La première étape s'est avérée riche et suffisante en elle-même pour approfondir notre compréhension de la circulation dans la baie. Le développement du modèle et sa calibration aurait probablement mérité aussi leur propre chapitre. Les expériences numériques menées à l'aide du modèle pour en extraire une compréhension du système auraient pu enfin être l'objet du troisième chapitre. Selon cette perspective, il est justifiable de se demander si le format du projet était bien adapté au cadre d'un programme de maîtrise, ou s'il aurait mieux convenu à celui d'un doctorat, avec les années supplémentaires qui lui sont propres. Après tout, plusieurs mémoires de maîtrises rédigés au même département montrent que l'analyse d'observations seule ou la modélisation seule a suffi à étoffer leurs pages.

Comme j'ai eu l'opportunité d'en faire l'expérience, même l'organisation d'une campagne de mesures de courte durée avec une équipe réduite nécessite une quantité de ressources, de gestion logistique et de planification qui laisse peu de place à la répétition dans le cadre d'un projet à courte échéance. Une mesure qui fait défaut ou qui manque à l'appel peut constituer un handicap sévère aux objectifs initiaux, coûtant du temps passé à chercher comment sauver les données, ou dans l'attente de reprendre la mesure. Plusieurs mois ont été perdus au cours de ce projet à tenter de sauver des mesures d'ADCP pour lesquelles le compas était fautif, par exemple. Pour ces raisons, un projet de maîtrise comportant de la récolte de données se doit d'être conservateur dans ses objectifs et dans ses échéances. Autrement,

le temps ne permet pas de réagir aux contingences et le projet peut devenir irréalisable.

Une évaluation critique de faisabilité est d'autant plus importante lorsque les conclusions d'un projet sont attendues par des projets parallèles. Il était prévu que d'autres étudiants du partenariat CHONe utilisent des sorties du modèle hydrodynamique de la BSI dans le cadre de leurs analyses. L'abandon de notre volet de modélisation a sans doute eu des répercussions sur ces projets. Si l'aspect de recherche collaborative aurait enrichit ce projet, il va sans dire qu'il contribuait aussi à gonfler son ampleur à des proportions ambitieuses.

Résultats clés

La contribution notable de cette étude est de dresser la description existante la plus complète de l'hydrodynamique de la BSI, dans la limite de ce que permettent les observations collectées. Corrélés à R=0.99 tout au long de l'été, la salinité constitue un bon prédicteur de la densité. La crue printanière cause une perturbation de la stratification dont les effets sont surtout sentis dans les 20 m sous la surface. À l'intérieur de cette perturbation, la densité peut varier jusqu'à 25% de sa moyenne estivale. Le pic de cette perturbation dure environ un mois et il était centré sur la première semaine de juin pour l'été 2017. Le minimum de salinité dans la BSI s'est produit 14±14, 22±14 et 23±14 jours après les maximums de débits climatologiques de la rivière des Rapides, du fleuve Saint-Laurent et de la rivière Moisie. Le volume d'eau douce requis pour produire ce minimum peut être fourni par les tributaires de la BSI en moins de 14 jours. Les données CTDs en tandem avec les données d'ADCP en route ont permis l'estimation du temps de résidence de la BSI selon 3 méthodes différentes, pour différentes conditions de marnage. Les 3 méthodes convergent vers un temps de résidence de l'ordre de $\tau = 2 - 12$ jours. La stratification réduite N_r, étudiée pendant un cycle de marée montre la pycnoline de l'embouchure située en moyenne à 9±1 m.

Lorsque moyennée à l'embouchure sur un cycle de marée, la dynamique observée était estuarienne. L'eau saumâtre coule vers l'aval dans les 5 m de surface, et coule principalement

vers l'amont sous 15 m de profondeur. Près de l'embouchure des rivières au nord de la BSI, se trouve une zone de faible profondeur où les courants de la baie n'ont que très rarement mené nos bouées GPS. Les bouées GPS posées dans cette zone ont été rapidement évacuées, suggérant que la circulation y est dirigée principalement vers l'aval. 22/46 bouées se sont échouées sur les berges ouest et sud de la BSI, montrant que les courants de surface y sont souvent dirigés. Un parallèle peut être noté entre ce comportement et 2 des 3 directions dominantes de vent identifiées (NNW et ESE), particulièrement en sachant que le cap des dérives était orienté en moyenne à 24±39° à l'ouest de celui du vent. Les courants de surface ont exhibé des vitesses moyennes de 17.4 cm s^{-1} et une vitesse maximale de 86.6 cm s^{-1}. Un courant longeant les berges ouest et sud pour sortir de la BSI près de Pointe à la Marmite a été observé au moyen de bouées GPS, et apparaît aussi tout au long du cycle de marée mesuré à l'embouchure.

Un regard critique a été posé sur le modèle conceptuel de la circulation dans la BSI proposé par Roche (2000). Puisque ce modèle est qualitativement en contradiction avec certaines de nos mesures, une réflexion vers un nouveau modèle est initiée. Nos mesures montrent qu'un nouveau modèle doit :

- avoir deux couches, dont la première occupe les 9 mètres de surface.
- comporter une géométrie circulaire pour la couche de surface.
- comporter une géométrie rectiligne pour la couche de fond.
- comporter une circulation estuarienne à l'embouchure en moyenne.
- expliquer une circulation cyclonique au jusant en moyenne.
- expliquer une circulation anti-cyclonique au flot à l'occasion.

Les courants observés semblent être la somme d'une interaction complexe entre les forçages du vent, de la marée et de la topographie. Le rayon interne de Rossby L_D a été calculé à 2.8 et 6.8 km en conditions peu et très stratifiées respectivement. Ceci suggère que son influence ne peut pas être écartée en surface, même si aucune de ses manifestations n'a été remarquée parmis les données récoltées. Comme les dimensions de la BSI diminuent

en profondeur, les phénomènes reliés à l'accélération de Coriolis ne sont attendus que en conditions faiblement stratifiées.

Limites du projet

Malgré l'effort de mesure déployé, il reste beaucoup à faire pour observer la pleine variabilité de l'hydrodynamique de la baie de Sept-Îles. Les CTDs des trois transects de 12 h répétés à l'embouchure montrent une évolution différente de la stratification au cours d'un cycle de marée. Il est probable que plusieurs mesures des courants selon cette méthodologie fournissent aussi des résultats dissimilaires. Une dynamique différente des courants pourrait être mesurée à l'embouchure de la BSI en lien avec la variablité saisonnière de stratification, mais aussi en lien avec la variabilité quotidienne des conditions de forçage. Quantifier ces variations nécessiterait une répétition de la mesure.

Une seule séries de mesures d'ADCP nous permet d'observer le courant dans la BSI en 3D. Cette mesure (Figure 19) n'a été prise qu'en période de flot. Obtenir aussi un transect d'ADCP en route pendant la période de jusant permettrait de solidifier les conclusions tirées de la mesure au flot soit, que l'hydrodynamique de la surface et du fond peuvent être simultanément différentes, et que ces différences semblent liées à la topographie. Avoir une mesure des deux phases les plus actives de la marée permettrait aussi d'approfondir notre compréhension de l'influence de la marée sur les courants en surface et en profondeur à différents endroits dans la BSI.

L'ensemble des données présentées ici ne traite enfin que de la circulation dans la BSI pendant la période estivale. L'influence des conditions hivernales de la stratification ou de la présence de glace sur la stratification demeure donc inconnue.

Perspectives de recherche

Pour surmonter les limites de cette étude, plusieurs options sont possibles. Une répétition des mesures à plus haute fréquence temporelle permettrait de séparer les conditions typiques des conditions passagères, mais serait coûteuse en ressources. Le déploiement de mouillages océanographiques permettrait de bien résoudre la variabilité temporelle, mais ne pourrait mener qu'à des conclusions localisées. L'option la plus plausible serait de poursuivre le projet tel que planifié à son départ et d'avoir recours à la modélisation. Les données récoltées au cours de ce projet sont accessibles dans les archives de Québec-Océan et devraient aider à la calibration du modèle.

RÉFÉRENCES

Baird, 2005. Wind-wave climate project feasibility study Moisie River. Tech. rep., Prepared for CDA engineering LTD.

Belles-Isles, M., Heppell, M., Bérubé, A., 2003. Programme décennal de dragage d'entretien des installations portuaires de la compagnie minière IOC à Sept-Îles Étude d'impact sur l'environnement déposée au ministère de l'Environnement. Rapport préparé par GENIVAR pour la compagnie minière IOC, 84 pages + annexes.

Berens, P., 2009. CircStat: A Matlab toolbox for circular statistics. Journal of Statistical Software 31 (10).

Birk, S., Bonne, W., Borja, A., Brucet, S., Courrat, A., Poikane, S., Solimini, A., Van De Bund, W., Zampoukas, N., Hering, D., 2012. Three hundred ways to assess Europe's surface waters: An almost complete overview of biological methods to implement the Water Framework Directive. Ecological Indicators 18, 31–41.

Bourgault, D., Koutitonsky, V. G., Bourgault, D., 1999. Real-time monitoring of the freshwater discharge at the head of the St. Lawrence Estuary. Atmosphere - Ocean 37 (2), 203–220.

Codiga, D., 2011. UTide - Unified Tidal Analysis and Prediction Functions. Tech. rep., Graduate School of Oceanography, University of Rhode Island, Narraganset, RI.

Cyr, F., Bourgault, D., Galbraith, P. S., 2011. Interior versus boundary mixing of a cold intermediate layer 116 (October), 1–12.

Du, J., Shen, J., 2016. Water residence time in Chesapeake Bay for 1980 – 2012. Journal of Marine Systems 164, 101–111.

Dyer, K. R., 1973. Estuaries: a physical introduction, 2nd Edition. Wiley.

Friedrichs, C. T., Aubrey, D. G., 1996. Uniform bottom shear stress and equilibrium hyposometry of intertidal flats. In: Pattiaratchi, C. (Ed.), Mixing in estuarine and coastal seas. Vol. 50. Coastal and estuarine studies, pp. 405–429.

Galbraith, P., Pettipas, R., Chassé, J., Gilbert, D., Larouche, P., Pettigrew, B., Gosselin, A., Devine, L., Lafleur, C., 2017. Physical Oceanographic Conditions in the Gulf of St. Lawrence in 2016. Can. Sci. Advis. Sec. Res. Doc. (2017/044), v + 69 p.

Galbraith, P. S., 2006. Winter water masses in the Gulf of St. Lawrence. Journal of Geophysical Research: Oceans 111 (6).

Gerkema, T., Zimmerman, J., 2008. An introduction to internal waves. Lecture Notes, Royal NIOZ, Texel, 207.

Gillett, D. J., Weisberg, S. B., Grayson, T., Hamilton, A., Hansen, V., Leppo, E. W., Pelletier, M. C., Borja, A., Cadien, D., Dauer, D., Diaz, R., Dutch, M., Hyland, J. L., Kellogg, M., Larsen, P. F., Levinton, J. S., Llansó, R., Lovell, L. L., Montagna, P. A., Pasko, D., Phillips, C. A., Rakocinski, C., Ranasinghe, J. A., Sanger, D. M., Teixeira, H., Van Dolah, R. F., Velarde, R. G., Welch, K. I., 2015. Effect of ecological group classification schemes on performance of the AMBI benthic index in US coastal waters. Ecological Indicators 50, 99–107.

Greenlaw, M. E., Roff, J. C., Redden, A. M., Allard, K. A., 2011. Coastal zone planning: A geophysical classification of inlets to define ecological representation. Aquatic Conservation: Marine and Freshwater Ecosystems 21 (5), 448–461.

Halpern, B. S., Longo, C., Hardy, D., McLeod, K. L., Samhouri, J. F., Katona, S. K., Kleisner, K., Lester, S. E., Oleary, J., Ranelletti, M., Rosenberg, A. A., Scarborough, C., Selig, E. R., Best, B. D., Brumbaugh, D. R., Chapin, F. S., Crowder, L. B., Daly, K. L., Doney, S. C., Elfes, C., Fogarty, M. J., Gaines, S. D., Jacobsen, K. I., Karrer, L. B., Leslie, H. M., Neeley, E., Pauly, D., Polasky, S., Ris, B., St Martin, K., Stone, G. S., Rashid Sumaila, U., Zeller, D., 2012. An index to assess the health and benefits of the global ocean. Nature 488 (7413), 615–620.

Halpern, B. S., Walbridge, S., Selkoe, K. A., Kappel, C. V., Micheli, F., D'Agrosa, C., Bruno, J. F., Casey, K. S., Ebert, C., Fox, H. E., Fujita, R., Heinemann, D., Lenihan, H. S., Madin, E. M., Perry, M. T., Selig, E. R., Spalding, M., Steneck, R., Watson, R., 2008. A global map of human impact on marine ecosystems. Science 319 (5865), 948–952.

Healy, T., Harada, K., 1991. Definition and physical characteristics of the world's enclosed coastal seas. Marine Pollution Bulletin 23 (C), 639–644.

Hein, F. J., Syvitski, J. P. M., Dredge, L. A., Long, B. F., 1993. Quaternary sedimentation and marie placers along the North Shore, Gulf of St. Lawrence; and Reply. Canadian Journal Earth Sciences 31 (1), 222+.

Hir, P. L., Roberts, W., Cazaillet, O., Christie, M., Bassoullet, P., Bacher, C., 2000. Characterization of intertidal flat hydrodynamics. Continental Shelf Research 20, 1433–1459.

Holloway, P. E., 1996. A Field Investigation of Water Exchange Between a Small Coastal Embayment and an Adjacent Shelf. In: Pattiaratchi, C. (Ed.), Mixing in estuarine and coastal seas. Vol. 50. Coastal and estuarine studies, pp. 145–158.

Hutter, K., Wang, Y., Chubarenko, I. P., 2011. Physics of Lakes. Vol. 2. Springer-Verlag Berlin Heidelberg.

Koutitonsky, V. G., Long, B. F., 1991. Rivière Moisie. Étude du milieu physique de l'estuaire. Vol. N. 6: Dynamique de l'estuaire. Section A: Hydrodynamique.

Kundu, P. K., 1976. A note on Ekman veering observed near the ocean bottom. Journal of Physical Oceanography 6, 238–242.

Kundu, P. K., Allen, J. S., Smith, R. L., 1975. Modal Decomposition of the Velocity Field near the Oregon Coast. Journal of Physical Oceanography 5 (4), 683–704.

Llebot, C., Rueda, F. J., Solé, J., Artigas, M. L., Estrada, M., 2014. Hydrodynamic states in a wind-driven microtidal estuary (Alfacs Bay). Journal of Sea Research 85, 263–276.

Martins, C. S., Hamann, M., Fiúza, A. F. G., 2002. Surface circulation in the eastern North Atlantic, from drifters and altimetry. Journal of Geophysical Research: Oceans 107 (C12), 10–1–10–22.

Matte, P., Secretan, Y., Morin, J., 2014. Quantifying lateral and intratidal variability in water level and velocity in a tide-dominated river using combined RTK GPS and ADCP measurements. Limnology and Oceanography: Methods 12 (MAY), 281–302.

Milbrandt, J. A., Bélair, S., Faucher, M., Vallée, M., Carrera, M. L., Glazer, A., 2016. The Pan-Canadian High Resolution (2.5 km) Deterministic Prediction System. Weather and Forecasting 31 (6), 1791–1816.

Neumeier, U., Joly, S., 2014. Mesures des vagues, des courants et des glaces de 2010 à 2014 dans l'estuaire et le golfe du Saint-Laurent pour les problèmes d'érosion côtière, Rapport préparé pour le ministère de la Sécurité publique. Université du Québec à Rimouski, 88.

Pedlosky, J., 1987. Geophysical Fluid Dynamics. Springer-Verlag New York Inc.

Procéan, 1999. Projet de développement du Terminal de vrac - Pointe Noire, étude environnementale. Tech. rep., Corporation du port de Sept-Îles.

Richardson, P. L., 1983. Eddy Kinetic Energy in the North Atlantic From Surface Drifters. Journal of Geophysical Research 88 (C7), 4355–4367.

Roche, 1991. Étude d'impact sur l'environnement, projet décannal de dragage d'entretien des installation portuaires de la compagnies IOC à Sept-Îles. Tech. rep., Rapport final.

Roche, 2000. Suivi des circulations et des panaches de turbidité lors du dragage de 1999. rapport présenté à l'administration du Port de Sept-Îles, 83.

Safak, I., Wiberg, P. L., Richardson, D. L., Kurum, M. O., 2015. Controls on residence time and exchange in a system of shallow coastal bays. Continental Shelf Research 97, 7–20.

Talley, L. D., Pickard, G. L., Emery, W. J., Swift, J. H., 2011. Descriptive physical oceanography: an introduction, sixth edit Edition. Elsevier.

Zhu, J., Weisberg, R. H., Zheng, L., 2015. On the Flushing of Tampa Bay. Estuaries and coasts 38, 118–131.

ANNEXE A

ADCP COMPASS CORRECTION SCHEMES

Introduction

Ancillary data properly describing the orientation of an acoustic Doppler current pro-filer (ADCP) is paramount to extracting interpretation from the observations. Several situations can occur at sea which adversely affect the quality of this data, especially when the ADCP is not mounted to the ship's hull. As part of sampling in the Bay of Sept-Îles (BSI), five underway ADCP measurements were conducted as summarized in Table 8, where heading data is contaminated. This appendix details the two strategies used to correct for this contamination, and their varying degree of success.

Dates (dd/mm/yyyy)	Bin size (m)	Mode	Bottom track	Transect	Contamination
20/06/2017	0.5	Self contained	No	T1	Yes
21/06/2017	0.5	Self contained	No	-	Yes
24/09/2017	0.5	Self contained	No	T1	Yes
16/05/2018	0.5	Real time	Yes	T2	No
17/05/2018	0.5	Real time	Yes	T1	Yes

Table 8: Summary of underway ADCP measurement parameters. All measurements used a Teledyne RDI Sentinel V 500 kHz profiler. Measurement from 21/06/2017 is not shown here. It was conducted in the shallow parts of the bay following the shore in the clockwise direction.

We define θ_p, θ_t, and θ_b, respectively the headings measured by the ADCP's compass, the heading representative of it's true orientation, and the heading representative of the boat's

orientation. We also define the earth frame of reference R, the ADCP's frame of reference R', and the convention that primed variables are measured in R'.

With bottom track

First we examine the contaminated data from May 2018. This sampling was conducted using bottom track and logging navigation data from the ship's inertial central. This means that θ_b and θ_p should be the same if the towing body swims parallel to the boat, but no rigid link prevents them from being different. It was noticed that velocity profiles were unusually hard to interpret and hypothesized the wave action felt during measurements was frequently forcing the towing body out of alignment with the boat. Since bottom track and water velocities are measured in the same frame of reference, heading data is not needed to correct the data for boat movement, therefore good heading data is only needed to rotate water velocities from beam to earth coordinates, or rather in this case to complete the horizontal rotation by $\Delta\theta = \theta_t - \theta_p$. The challenge then reduces to finding the unknown θ_t, which may be done by computing the angle between a vector quantity measured both in R and R'.

Speed over ground is a candidate for this task as it is logged in R by the ship's inertial central or computed by the GPS track log, while it's exact opposite should be provided by the bottom track data, measured in R'. Figure 21 shows track log velocities in red with both directions along the transect on opposing sides of the near zero velocities associated to CTD stops. The bottom track velocities in blue, are of correct amplitude, but their heading is almost uniformly distributed.

Looking at the speed time series on figure 22, it is also apparent that the bottom track velocities are far less steady than those of the track log when both should be similar. It may also be noted that towards 16:48 UTC, one transect was done using the ADCP's internal compass and raw bottom track velocities from this line are in far better accordance with the GPS velocities in comparison to the rest of the data set.
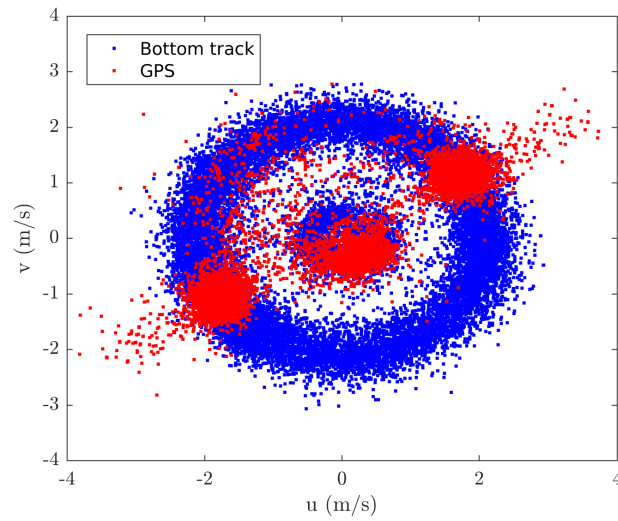
Figure 21: Comparison between speed deduced from the track log of 17/05/2018 and the opposite of bottom track velocities.

The middle panel shows the bottom track velocities rotated by $\Delta\theta$ as calculated using this method. The same time-dependent rotation is then applied to each individual ping before averaging. The currents measured during the 12 hour transects of May 17, 2018, averaged over 252 meters horizontally and over the 8 surface meters vertically, are show on figure 23. The left side panels display u_a and u_c without rotation by $\Delta\theta$ and the right side panels show the same with rotation.

The rotated speeds are notably smoother both along the individual transects and through time across them. Measurements began and ended during ebb tide, and this signal appears with improved clarity in the rotated speeds. Overall, this strategy appears to adequately determine the orientation of the towing body, bringing the velocity fields to a state where interpretation is legitimate.
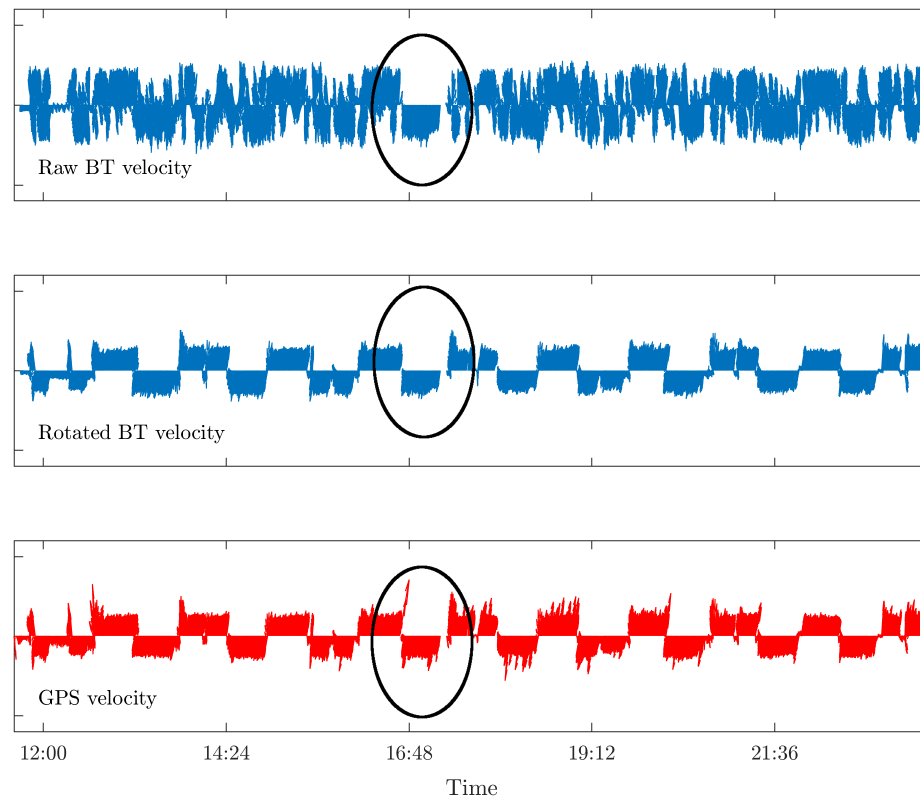
Figure 22: Stick plot time series of the opposite of the raw bottom track velocity (top), rotated bottom track (middle), and GPS velocities (bottom). The north velocity component points upwards and the eastward component points to the right. The section when the ADCP was used as a heading source is circled.

Without bottom track

Second we examine data from measurements along the same transect and during 12 hours in June and September 2017. These velocities differ from the previous data set in that they were collected without bottom tracking and rotated to earth coordinates using the ADCP's internal compass. It was first noticed that adding boat speed to raw velocities visibly did not cancel boat motion. Heading logged by the profiler was then noted to be different from that computed with the GPS track in a time varying way, see figure 24. Since velocities were
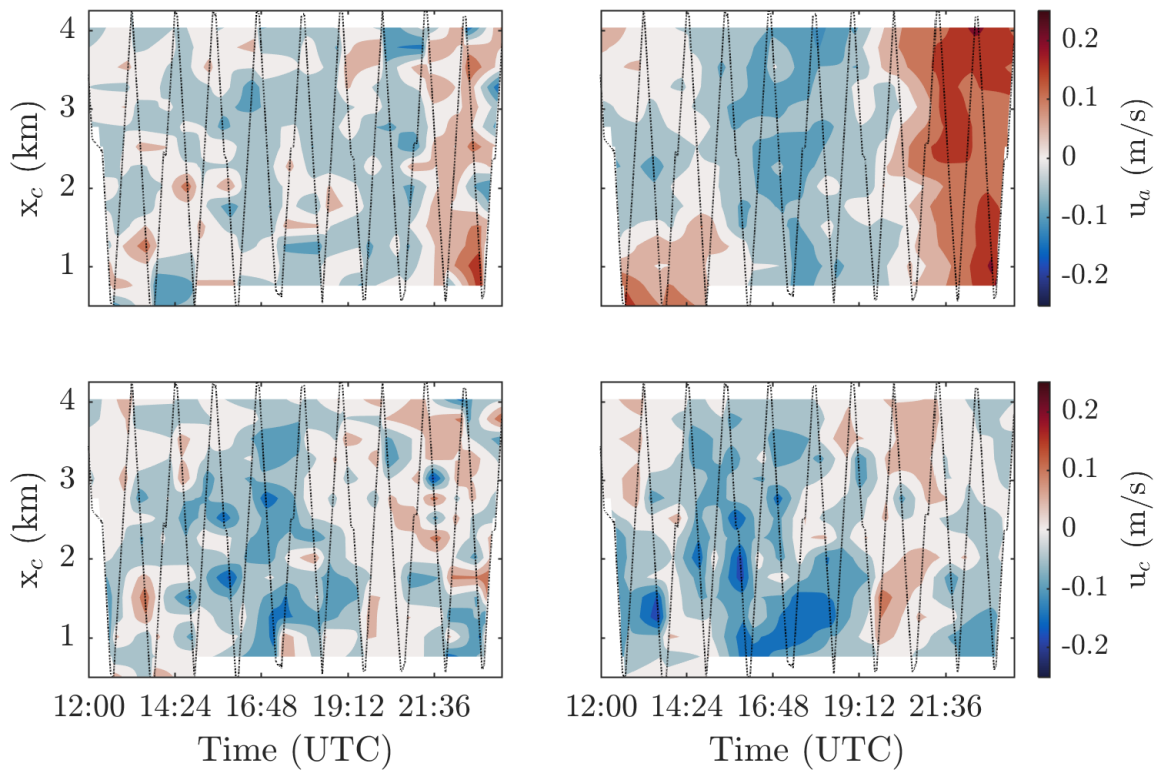
Figure 23: Measured ADCP along shore (top) and cross shore (bottom) velocities for the May 17 2018 transects. The left panels are raw, while the right have been rotated by $\Delta\theta$. Ship track is shown by the dotted line.

difficult to interpret and rotating by the difference between θ_p and θ_b showed no improvement, it was considered θ_p must be unrepresentative of the towing body's orientation. The objective is therefore again to determine θ_t. This task is complicated by the absence of bottom track data first because it cannot be used to determine θ_t, and second because precisely determining θ_t is critical to correcting velocities for boat motion since boat and water speeds must be added in the same frame of reference.

The assumption which is made here is that the boat's speed is much greater than the water velocities averaged over the whole water column. This may hold over sheared currents
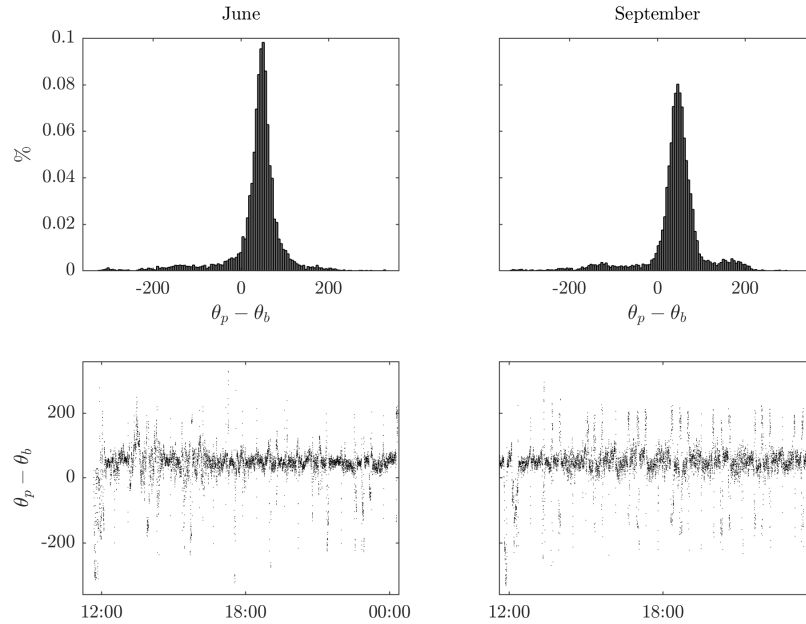
Figure 24: Statistical (top) and time series (bottom) representation of the difference between θ_p and θ_b for the repeated transects of June 20 (left) and September 25 (right), 2017.

or low current areas, but validity is limited by the boat's speed which must be kept at 4 kt. Under this assumption, raw measured velocity may be used to approximate speed over ground and again provide a quantity measured both in R and R', as shown by equation 2.1.

$$\mathbf{u}'_p = \mathbf{u}_p - \mathbf{u}'_b \approx -\mathbf{u}'_b = - \begin{bmatrix} \cos(\Delta\theta) & -\sin(\Delta\theta) \\ \sin(\Delta\theta) & \cos(\Delta\theta) \end{bmatrix} \mathbf{u}_b \qquad (2.1)$$

Before being rotated by $\Delta\theta$, the measurements presented here are filtered for correlation, error velocity and side lobe interference. Pings corresponding to boat speeds slower than 1.5 m/s are also removed. Vertically averaged speeds are then calculated and used to compute $\Delta\theta$. The rotation to earth coordinates is then completed and resulting u_p, v_p components are added to boat speed such as to remove influence of boat motion.

Following this process, appearance of many features observable in the data collected

with bottom track, such as a ~10 m thick surface layer, and uniform tidal movement in phase at a 90° lag with sea surface elevation suggest θ_t has been adequately determined for several pings. The results are however inhomogeneous, suggesting that the assumptions do break down in many cases. An additional step of quality control by inspection is therefore performed where are manually removed pings in abrupt discordance with their context and pings showing large speeds ($\geq$ 50 cm/s) uniform over the whole water column. Figure 25 shows along shore and cross shore velocities averaged horizontally over 500 m and vertically over the first 8 m for the June 2017 and September 2017 transects, following this step.
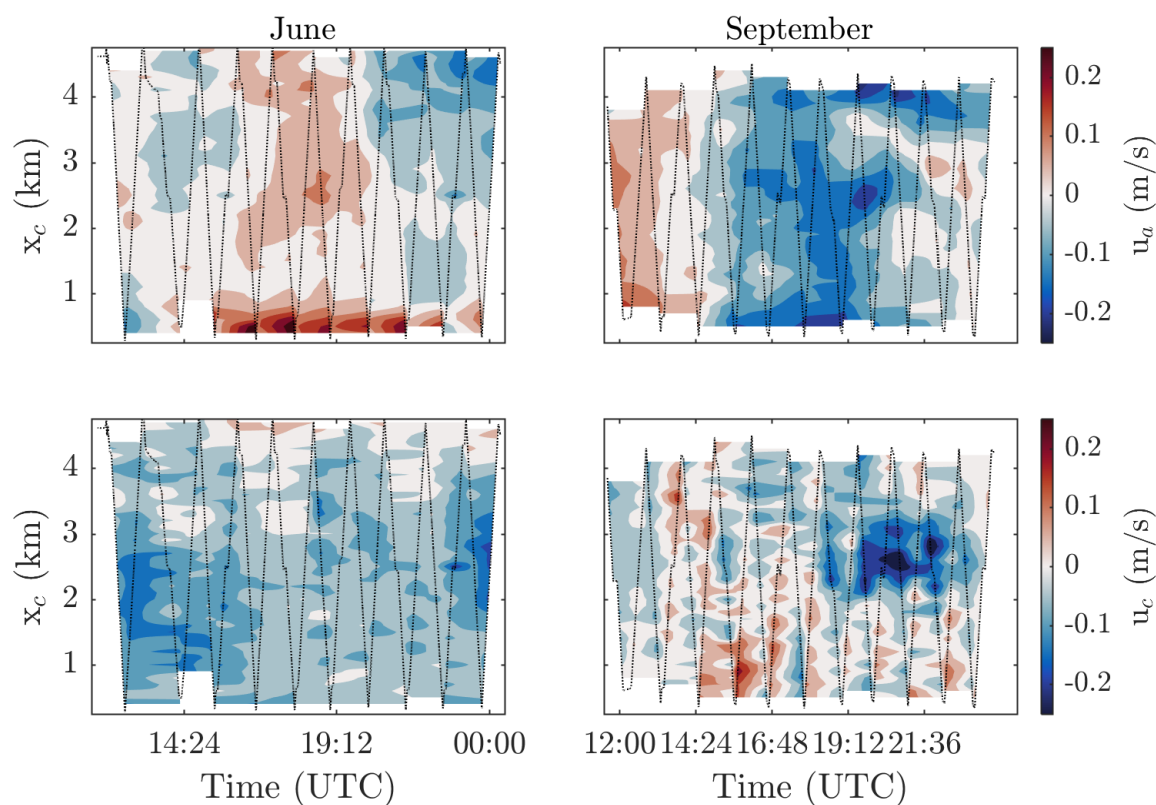

Figure 25: Measured ADCP along shore (top) and cross shore (bottom) velocities for the May (left) and September (right) transects. Ship track is shown by the dotted line.

While some features such as the tidal signal, and the speed magnitude scale, now appear

comparable to those found in bottom track data, other features suggests interpretations should be cautious. Speeds are often of opposite signs across boat turns, such as is most visible in the September cross shore velocity and to a lesser extent in the June along shore velocity. The bottom right panel of Figure 25 also shows speeds of alternating sign following the direction of boat movement, suggesting the influence of it's motion is not yet cancelled out.

It should be noted that these measurements were conducted over waters 30-70 m deep, where bottom track ADCP data shows frequent vertical shear. This condition helps the assumptions required for this method to be fruitful. It was also tried with very little success for the 21/06/2017 measurements conducted over 10-30 m, where shear is less of a guarantee.